Ion- Exchange of Zeolitic Brønsted Acid Sites with Metal Cations Influences the Hydrocarbon Pools (HCP) during Tandem CO_2 Hydrogenation

Fatima Mahnaz[1], Balaji C. Dharmalingam[2], Jasan Robey Mangalindan[1], Jenna Vito[1], Jithin John Varghese[2] & Manish Shetty[1*]

[1]Artie McFerrin Department of Chemical Engineering, Texas A&M University College Station, TX 77843.

[2]Department of Chemical Engineering, Indian Institute of Technology Madras, Chennai, Tamil Nadu 600036 India.

*Corresponding Author: manish.shetty@tamu.edu

Abstract

We demonstrate that the exchange of zeolitic Brønsted acid sites (BAS) with cations from metal-oxides plays a pivotal role in the propagation of hydrocarbon pools (HCP) during CO_2 hydrogenation. We estimated the likelihood of cationic species migration from different oxides-In_2O_3, $ZnZrO_x$, Cr_2O_3 and their exchange with BAS by computing metal vacancy formation energies. Accordingly, we integrated metal-oxides and SAPO-34 at nanoscale proximity (~1400 nm), to probe the propensity of the cations to exchange with BAS. To assess the influence of ion-exchange on HCP, we measured propylene-to-ethylene ratio (indicates relative propagation of olefin to aromatic cycles) and paraffin-to-olefins ratio, which revealed that $In^{\delta+}$ species inhibited HCP propagation while $Zn^{\delta+}$ species enhanced hydrogen transfer. Combining reactivity data with ammonia temperature programmed desorption, occluded hydrocarbon analysis, ^{13}C solid-state nuclear magnetic resonance and X-ray photoelectron spectroscopy analysis, we provide insights into the influence of ion-exchanged species on HCP for rational integration of bifunctional catalysts.

Keywords

Tandem hydrogenation, methanol, zeolite, hydrocarbon pool, MTO, C-C coupling, ion-exchange, Brønsted acid sites

1. Introduction

The 2050 reaction engineering roadmap suggests catalysis research to focus on i) the use of nontraditional chemical feedstocks such as CO_2, biomass, end-of-life plastics, and ii) the development of sustainable catalytic paths to establish carbon-neutral processes.[1] In this regard, anthropogenic CO_2 can be considered to be the next source of carbon for utilization as a feedstock in the chemical industry.[1] Among various

pathways for carbon dioxide utilization (CDU) techniques, the tandem hydrogenation of CO_2 to olefins using "green hydrogen" offers a sustainable route to synthesize potentially carbon-neutral platform chemicals for polymer and plastic industries.[2-4] The reaction combines two steps: i) methanol (CH_3OH) synthesis from CO_2 and H_2 over the oxygen vacancies/redox sites of a reducible metal oxide, and ii) subsequent conversion of methanol-to-olefins (MTO) over Brønsted acid sites (BAS) of zeolites/zeotypes in a single reactor.[3, 5-8] Although the concept seems appealing, molecular understanding of the complex interactions of different active sites with the reactants and intermediates during the reaction is yet unclear. In our recent study, we observed that the efficacy of bifunctional oxide/zeolite systems depends largely on the effective transfer and consumption of the intermediate CH_3OH, which could be improved by increasing the proximity between redox sites and BAS in the bifunctional system.[9] Therefore, hydrocarbon (HC) yield was enhanced by improving advective transfer of CH_3OH from redox sites to BAS by reducing their spatial distance. However, at nanoscale distance, the catalytic performance of bifunctional systems could be hindered by cation migration and their exchange with BAS under harsh reaction conditions,[10, 11] especially for In_2O_3 and zeolite admixtures.[10, 12-15] Several attempts have been made to prevent ion exchange of cations with BAS, e.g., coating zeolite with silicate-1 (S-1),[16] or coating metal oxide with Al_2O_3,[17] etc. While these methods prevent ion exchange (as no H^+ site present in the coating materials), cation migration could still occur under the harsh reaction conditions. In fact, In_2O_3 has been reported to form InO_x nanolayers by migrating over oxide supports (e.g., TiO_2, ZrO_2, MnO), which was found to be more reactive (~2-14× higher CO_2 conversion) than In_2O_3, as demonstrated by Wang et al.[18] As such, the catalytic activity of S-1 or Al_2O_3 coated zeolite or metal oxide could be affected by the reactivity of migrated cations. Hence, material design for CO_2 hydrogenation is still impeded by the knowledge gap of how such migration can influence the reactivity of oxide/zeolite systems.

Furthermore, the complex reaction mechanism of CO_2 hydrogenation (coupling CH_3OH synthesis and MTO conversions), presents additional challenges in material design. Specifically, MTO mechanism includes a series of reactions such as the formation of C-C bond, formation of lower olefin, olefin methylation, olefin cracking, olefin aromatization, aromatic methylation, aromatic dealkylation to olefin, formation of paraffins by hydrogen transfer (HT), and the formation of co-catalytic intermediates within olefin and aromatic cycles of the "hydrocarbon pool (HCP)" mechanism (see **Figure 1**).[19] Considering the possibility of ion exchange of BAS with cations from metal oxides, the question remains if such exchange can create new active sites in the zeolite framework and influence these reactions steps. Specifically, ion-

exchanged zeolites have been proven to exhibit unique catalytic properties during methanol-to-hydrocarbon (MTH) conversion. For instance, ion exchange of BAS of HZSM-5 with zinc or gallium cations enhanced aromatization of olefins,[20] while ion exchange of BAS of β zeolite with iron, chromium and manganese cations enhanced oligomerization of lower olefins.[21] As such their influence on HCP under CO_2 hydrogenation conditions remains a missing link.

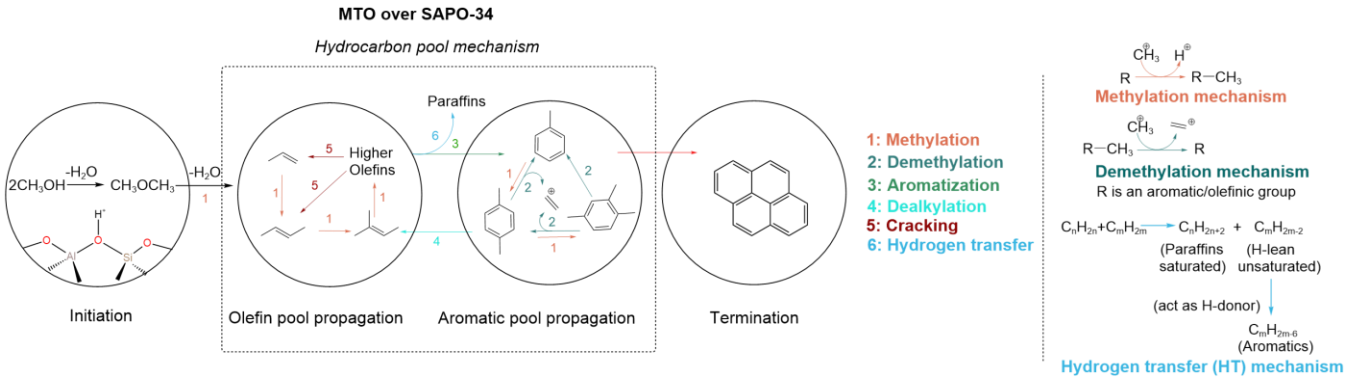

Figure 1: Hydrocarbon pool (HCP) mechanism of methanol-to-hydrocarbon (MTH) conversion on zeolites/zeotypes including initiation, propagation, and termination phases. The propagation encompasses multiple steps, including olefin methylation, cracking, hydrogen transfer, aromatization, aromatic methylation, and aromatic dealkylation. Adapted with permission from Ilias, S. & Bhan *et al*.[22] Copyright *J. Catal. 2012*.

Considering these knowledge gaps in understanding the propensity of metal oxides to form cations and the influence of their ion exchange with BAS on the reactivity of oxide/zeolite systems and HCP propagation during CO_2 hydrogenation, we aim to (1) find a descriptor to predict the likelihood of the migration of metal cations from different metal oxides to zeolite for their exchange with BAS, (2) probe the influence of different cations exchange with BAS on HC selectivity and space-time yields (STY), (3) explore whether these ion-exchanged species can create new active sites in the zeolite framework and influence HCP propagation under tandem reaction conditions. Accordingly, we selected three representative metal oxides e.g., In_2O_3, $ZnZrO_x$, and Cr_2O_3 for CH_3OH synthesis as these oxides have been frequently employed for CO_2 hydrogenation reactions,[6, 10, 23-27] and can provide valuable insights on how diverse metal oxides interact with zeolitic BAS. We integrated these metal oxides with SAPO-34, a silicoaluminophosphate of chabazite (CHA) topology with narrow eight-membered windows (3.8 × 3.8 Å) for MTO conversion, which favors the propagation of the olefin cycle leading to high selectivity towards light olefins by preventing the escape of large aromatic compounds.[25, 27-34] We deduced the

likelihood of migration of cations from the metal oxide lattice by computing metal vacancy formation energies using Density Functional Theory (DFT) simulations. Our estimation on the tendency of different metal oxides to form cationic species and their exchange with BAS was consistent with our experimental findings, where we strategically integrated redox sites of metal-oxides and BAS of SAPO-34 at nanoscale proximity as intrapellet admixtures (estimated distance ~1400 nm), for solid-state ion exchange (SSIE) to occur. To probe the influence of these ion-exchanged species on HCP, we assessed two performance metrics, propylene-to-ethylene (C_3/C_2) and paraffin-to-olefin (P/O) ratios during CO_2 hydrogenation, which convey the relative propagation of the olefin cycle to the aromatic cycle, and the degree of saturation of olefins in HCP, respectively.[35] Our analysis with C_3/C_2 and P/O ratios, coupled with the occluded HC analysis and ^{13}C solid-state nuclear magnetic resonance (ssNMR) spectroscopy revealed that ion exchange of BAS with $In^{\delta+}$ and $Zn^{\delta+}$ species influenced the olefin and aromatic pool propagation, consequently altering HC selectivity and yield. Overall, this study offers insights into the influence of different metal oxides and their cations on the catalytic performance of bifunctional oxide/zeolite systems and links the observed catalytic performance to the propagation of olefin and aromatic cycles in HCP during CO_2 hydrogenation.

2. Results and discussion

2.1. Cationic species migration

We selected three metal oxides e.g., In_2O_3, $ZnZrO_x$ (Zn:Zr molar ratio 1:4), and Cr_2O_3 for CO_2 to CH_3OH conversion, and SAPO-34 ((Al+P)/Si ratio 7.5) for MTO conversion. We note that the exchange of BAS with cations from metal oxides first necessitates their migration from the oxide to the BAS. Therefore, the likelihood of this migration could depend on the propensity of metal oxides to form cations. Hence, we calculated the metal vacancy formation energies of different metal oxides using Density Functional Theory (DFT) simulations, to estimate the propensity of metal cations being removed from the surface of metal oxides. The exposed surfaces of metal oxides were created with different possible terminations as slab models, based on their respective PXRD patterns (see **Figure S20**). The metal vacancy formation energy was found to vary based on the specific metal atom removed and their local coordination environment. Details on the estimation of metal vacancy formation energy is given in supplemental information **section S2.4**. Based on our analysis, the most favorable Cr removal from Cr_2O_3 had an energy penalty of 5.78 from the Cr_2O_3(110) surface while it was 3.98 eV for the removal of In from In_2O_3(100) surface (see **Table S8**). In the case of $ZnZrO_x$, Zn removal was substantially more facile than Zr removal,

with the $ZnZrO_x$(011) surface exhibiting the lowest metal vacancy formation energies of 1.03 eV. In contrast, Zr cation removal was found to be highly unlikely as the lowest energy penalty was 19.48 eV (see **Table S7**). These assessments indicate that the removal of $In^{\delta+}$ and $Zn^{\delta+}$ from In_2O_3 and $ZnZrO_x$, respectively, are more favorable than removal of $Cr^{\delta+}$ from Cr_2O_3 and $Zr^{\delta+}$ from $ZnZrO_x$, as depicted in **Figure 2**. Therefore, we infer that the likelihood of $In^{\delta+}$ and $Zn^{\delta+}$ species migration and their exchange with BAS is higher, as compared to $Cr^{\delta+}$.

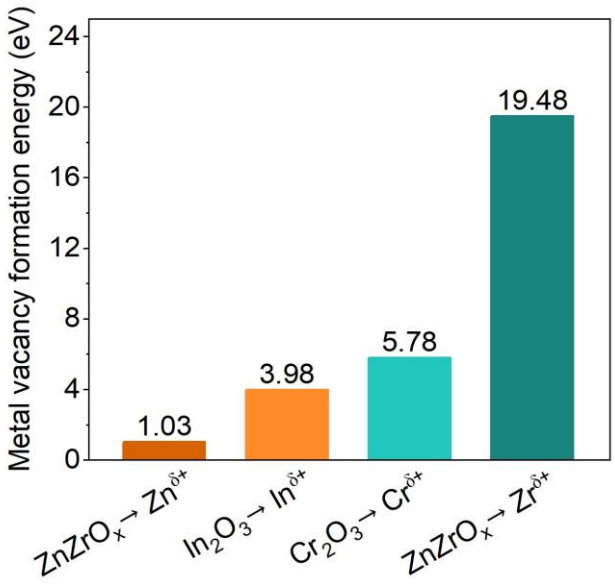

Figure 2: Metal vacancy formation energy of In_2O_3, $ZnZrO_x$ and Cr_2O_3 surfaces for the most favorable metal cation formation estimated by Density Functional Theory (DFT) simulations. The values in y-axis indicate metal vacancy formation energies for the removal of $Zn^{\delta+}$ from (110) facet of $ZnZrO_x$, $Cr^{\delta+}$ from (011) facet of Cr_2O_3, $In^{\delta+}$ from (100) facet of In_2O_3, and $Zr^{\delta+}$ from (002) facet of $ZnZrO_x$. Details on the surface formation energies of different facets with possible terminations (metal and O terminations) is given in **Table S6**.

The next question is whether the trend for the migration of cations ($Zn^{\delta+}$ (1 eV) > $In^{\delta+}$ (3.9 eV) > $Cr^{\delta+}$ (5.8 eV)) from metal oxides correlate with their tendency to exchange with BAS in SAPO-34. To verify, we integrated the metal oxides with SAPO-34 at nanoscale proximity (distance between redox sites and BAS ~1400 nm, estimated semi-quantitively by an iteration method, see **section S2.2**)[36] as intrapellet admixtures (denoted as intrapellet_In_2O_3/SAPO-34, intrapellet_$ZnZrO_x$/SAPO-34 and intrapellet_Cr_2O_3/SAPO-34) by mixing metal oxide and SAPO-34 in an agate mortar, allowing for solid-

state ion exchange (SSIE) of BAS to occur.[9] In addition, we deliberately ion exchanged the BAS of SAPO-34 with respective cations of the metal oxides via incipient wetness impregnation (IWI) (denoted as xM-SAPO-34 where, M=$In^{\delta+}$, $Zn^{\delta+}$, $Cr^{\delta+}$, etc. and x=M:Si ratio), to have a point of reference of how ion exchange of BAS with different cations influence the acidic properties of SAPO-34.[21] It is to be noted that we selected a M:Si molar ratio of 1 for ion exchanged xM-SAPO-34, as the intrapellet admixtures had M:Si≥1 (In:Si ≈ 5 in intrapellet_In_2O_3/SAPO-34, Zn:Si ≈ 1 in intrapellet_$ZnZrO_x$/SAPO-34 and Cr:Si ≈ 8 in intrapellet_Cr_2O_3/SAPO-34). The structural, textural and morphological properties of intrapellet admixture and ion-exchanged SAPO-34 are given in SI **section S3.2-3.5**.

For quantitative assessment of the acidity of SAPO-34 in intrapellet admixtures, we performed NH_3 temperature programmed desorption (NH_3-TPD), which revealed that SSIE likely occurred in intrapellet_In_2O_3/SAPO-34 and intrapellet_$ZnZrO_x$/SAPO-34, while not in intrapellet_Cr_2O_3/SAPO-34 (acid site density 0.38, 1.34 and 1.83 mmol/g, respectively, as compared to 1.95 mmol/g for SAPO-34 shown in **Figure 3A-C**) during the mixing process. However, for all ion-exchanged xM-SAPO-34, acid site density of SAPO-34 was drastically reduced by IWI (acid site density 0.19, 0.32 and 0.39 mmol/g in 1.0In-SAPO-34, 1.0Zn-SAPO-34 and 1.0Cr-SAPO-34, respectively, see **Figure 3A-C**).

To assess the likely oxidation states and electronic environment of the ion-exchanged species formed via SSIE and IWI, we conducted X-ray photoelectron spectroscopy (XPS) of intrapellet admixtures and xM-SAPO-34. **Figure 3D** shows that intrapellet_In_2O_3/SAPO-34 and 1.0In-SAPO-34 exhibited peaks at 443.9 and 451.4 eV corresponding to $In3d_{5/2}$ and $In3d_{3/2}$ of bulk In_2O_3. However, both exhibited additional peaks at higher B.E. for $In3d_{3/2}$ and $In3d_{5/2}$ at 445.2 and 452.7 eV, as compared to In_2O_3, likely indicating a stronger interaction of $In^{\delta+}$ species with SAPO-34.[10, 13, 37] We reported a similar observation previously for In_2O_3 and HZSM-5 (Si:Al ratio 40), where higher B.E peaks at 445.6 and 453.2 eV were observed due to SSIE of BAS with $In^{\delta+}$, likely forming In_2O moieties inside the zeolite framework.[9]

A similar shift of peaks to higher B.E. values was observed for intrapellet_$ZnZrO_x$/SAPO-34 and 1.0Zn-SAPO-34 at 1024.0 and 1047.4 eV (see **Figure 3E**), as compared to 1023.4 and 1046.1 eV for $Zn2p_{3/2}$ and $Zn2p_{1/2}$ corresponding of Zn^{2+} in bulk $ZnZrO_x$. These high B.E. peaks are likely indicative of a stronger interaction of $Zn^{\delta+}$ species with SAPO-34 framework.[38, 39] Several studies attributed the shift of this peak for $Zn^{\delta+}$ to the formation of $Zn^{2+}(O^-)_2$ associated with the zeolite framework.[38, 40, 41] Additionally,

we did not observe any shift in the B.E. for Zr $3d_{3/2}$ and Zr $3d_{5/2}$ in intrapellet_$ZnZrO_x$/SAPO-34, indicating that ion exchange of BAS with $Zr^{\delta+}$ likely did not occur (see **Figure S27**), consistent with its higher metal vacancy formation energies estimated by DFT (**Table S8**).[42]

Unlike intrapellet_In_2O_3/SAPO-34 and intrapellet_$ZnZrO_x$/SAPO-34, intrapellet_Cr_2O_3/SAPO-34 did not exhibit any higher B.E. peaks (exhibited peaks only at 576.5 and 585.6 eV for $Cr2p_{3/2}$ and $Cr2p_{1/2}$ corresponding to bulk Cr_2O_3, see **Figure 3F**), indicating that likely no SSIE occurs between BAS and $Cr^{\delta+}$. However, 1.0Cr-SAPO-34 exhibited peaks at higher B.E of 577.9 and 588.0 eV, indicating possible ion exchange of BAS with $Cr^{\delta+}$. This is consistent with its reduced acid site density ~0.39 mmol/g as quantified by NH_3-TPD. This further confirms that SSIE did not occur in intrapellet_Cr_2O_3/SAPO-34 as the peak shift towards higher B.E. was not observed. From these observations, we deduce that the likelihood of forming cations ($Zn^{\delta+}$ (1 eV) > $In^{\delta+}$ (3.9 eV) > $Cr^{\delta+}$ (5.8 eV)) aligns with their tendency to exchange with BAS at nanoscale proximity.

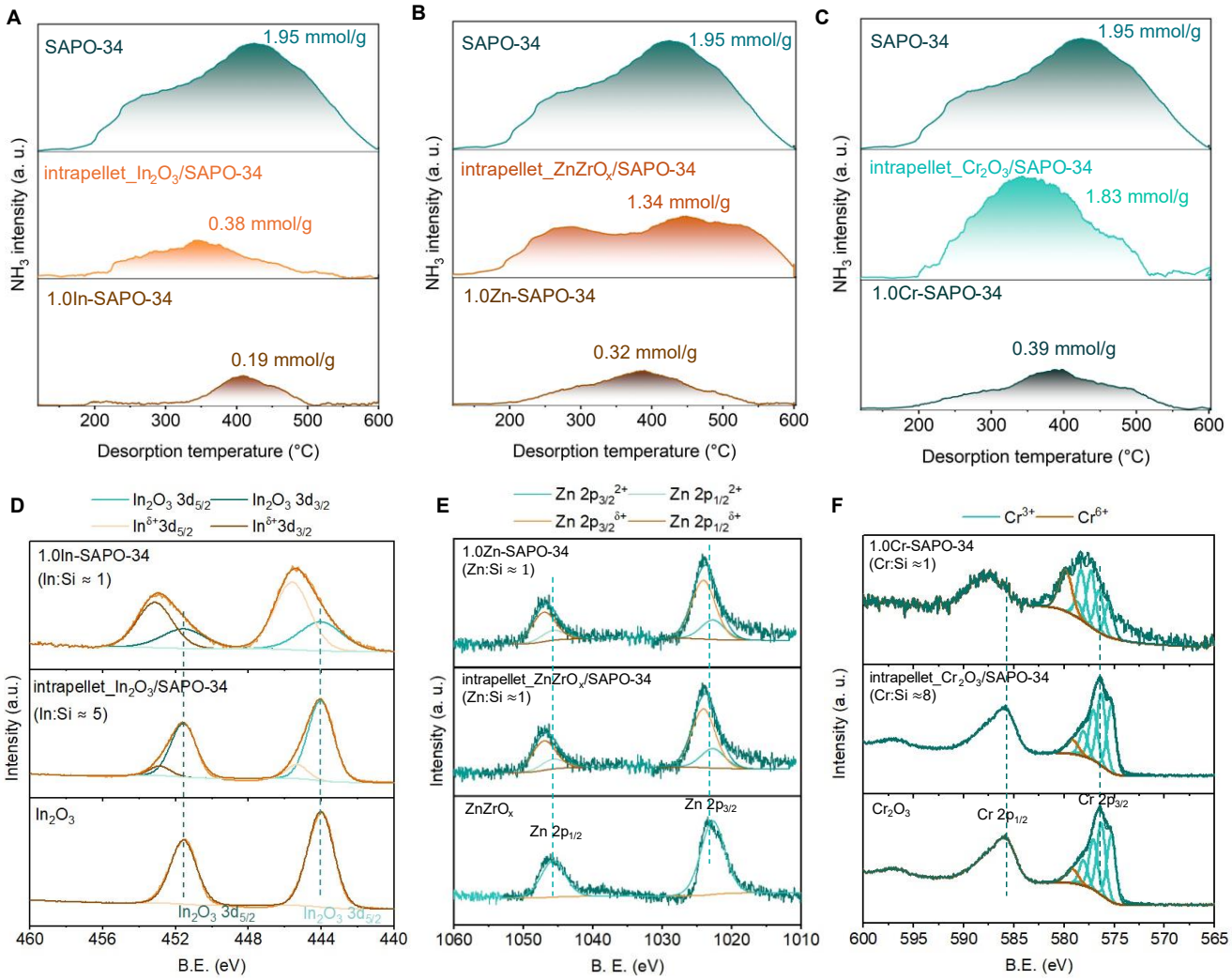

Figure 3: Probing ion exchange of Brønsted acid sites (BAS) of SAPO-34 with cationic species. Ammonia temperature programmed desorption (NH_3-TPD) profiles for A) intrapellet_In_2O_3/SAPO-34, 1.0In-SAPO-34 and SAPO-34, B) intrapellet_$ZnZrO_x$/SAPO-34 and 1.0Zn-SAPO-34 and C) intrapellet_Cr_2O_3/SAPO-34 and 1.0Cr-SAPO-34. D) X-ray photoelectron spectroscopy (XPS) of pristine In_2O_3, intrapellet_In_2O_3/SAPO-34 and 1.0In-SAPO-34; E) XPS of pristine $ZnZrO_x$, intrapellet_$ZnZrO_x$/SAPO-34 and 1.0Zn-SAPO-34. F) XPS of pristine Cr_2O_3, intrapellet_Cr_2O_3/SAPO-34 and 1.0Cr-SAPO-34. It is to be noted that we selected ion-exchanged SAPO-34 (denoted as xM-SAPO-34 where, M=$In^{\delta+}$, $Zn^{\delta+}$, $Cr^{\delta+}$, etc. and x=M:Si ratio) with M:Si molar ratio of 1 for XPS, as the intrapellet admixtures had M:Si≥1 (In:Si ≈ 5 in intrapellet_In_2O_3/SAPO-34, Zn:Si ≈ 1 in intrapellet_$ZnZrO_x$/SAPO-34 and Cr:Si ≈ 7 in intrapellet_Cr_2O_3/SAPO-34).

2.2. Probing the influence of ion exchange of BAS with cations from metal oxides on the reactivity of oxide/SAPO-34 systems

Prior to assessing the impact of ion exchange of BAS on reactivity, it is imperative to understand how the reaction would proceed when ion exchange does not occur. Hence, we integrated metal oxides and SAPO-34 as interpellet admixtures where redox sites and BAS were integrated at a microscale proximity (~303 μm, as shown in **Table S2**) by physically mixing granules of oxides and SAPO-34.[9] NH_3-TPD revealed that likely no ion exchange occurred at microscale proximity (acid site density 2.1, 1.9, and 2.1 mmol/g in interpellet_In_2O_3/SAPO-34, interpellet_$ZnZrO_x$/SAPO-34 and interpellet_Cr_2O_3/SAPO-34, respectively, as compared to 1.95 mmol/g in SAPO-34, shown in **Figure S26**). As such, all three systems exhibited minimal deactivation during tandem CO_2 hydrogenation, as shown in **Figure S8-S10**. Furthermore, **Figure 4A** depicts that CO_2 conversion over interpellet admixtures remained stable with increasing cumulative turnover number (TON) where TON is defined as the total amount of carbon atoms observed in the products normalized by the total BAS in the catalyst.[44] This observation is consistent with our recent study for interpellet_In_2O_3/SAPO-34 system where minimal deactivation was observed during tandem CO_2 hydrogenation. However, an inherent drawback of SAPO-34 is its tendency to deactivate rapidly via coking during MTO, as shown in **Figure 4B** (1^{st} order deactivation rate constants during MTO and CO_2 evolution from spent SAPO-34 during temperature-programmed oxidation are shown in **Figure S1)**. We attributed the stable CO_2 conversion over interpellet_In_2O_3/SAPO-34 to the presence of H_2 during the reaction, which likely promoted olefin hydrogenation and interrupted olefin aromatization, thereby reducing the formation of deactivation-inducing polycyclic aromatics.[43] To assess if the presence of H_2 could also dominate the catalytic activity of interpellet_$ZnZrO_x$/SAPO-34 and interpellet_Cr_2O_3/SAPO-34 systems, we compared their performance with SAPO-34 (during MTO, without any H_2 co-feed) at similar TON. As shown in **Figure 4C**, at a cumulative TON ~850 mol_C/mol_{H+}, paraffin (C_2^0-C_4^0) selectivity was higher over interpellet admixtures (15%, 10%, and 17% over interpellet_In_2O_3/SAPO-34, interpellet_$ZnZrO_x$/SAPO-34 and interpellet_Cr_2O_3/SAPO-34, respectively), as compared to SAPO-34 (C_2^0-C_4^0 ~6% during MTO). Accordingly, the cumulative paraffin-to-olefin (P/O) ratio was ~2-3× higher over interpellet admixtures (P/O~0.15-0.21), as compared to SAPO-34 (P/O~0.07) in **Figure 4D**, indicating the degree of saturation of olefins was higher during CO_2 hydrogenation.

We note that paraffins could form via i) HT mechanism where the formation of hydrogen-lean aromatics causes the formation of a stoichiometric amount of paraffins to maintain the equilibrium of the HCP during MTO (see **Figure 1**), and/or ii) secondary hydrogenation of olefins to paraffins in the presence of H_2. Therefore, to probe the likely mechanism of the paraffin formation, we evaluated cumulative C_3

(propane+propylene)/C_2 (ethane+ethylene) ratio which indicates the relative propagation of olefin to aromatic cycle, since propylene predominantly comes from the olefin cycle,[22] and ethylene exclusively comes from the aromatic cycle as a terminal product.[35, 45] Furthermore, we note that olefins saturate in the presence of H_2.[46] Therefore, we considered the cumulative C_3/C_2 ratio rather than the cumulative $C_3^=/C_2^=$ ratio to holistically quantify the propylene and ethylene coming out of olefin and aromatic cycles, respectively.[43] As shown in **Figure 4D**, C_3/C_2 was higher over the three interpellet admixtures (3, 3.1 and 2.8 over interpellet_In_2O_3/SAPO-34, interpellet_$ZnZrO_x$/SAPO-34 and Cr_2O_3/SAPO-34), as compared to SAPO-34 (C_3/C_2~2.5), indicating the propagation of olefin cycle was more favored in the presence of H_2 (further corroborated by MTO with H_2 co-feed , shown in **Figure S4**). Therefore, we deduce that paraffins were likely formed *via* secondary hydrogenation, rather than HT, as otherwise C_3/C_2 ratio would have decreased by favoring the aromatic cycle since aromatics are the hydrogen-donor in HT mechanism (shown in **Figure 1**).

To further confirm our hypothesis, we performed occluded HC analysis (mass chromatogram shown in **Figure S28-S31**) to identify the coke species formed in SAPO-34 during MTO and CO_2 hydrogenation, respectively. **Figure 4E** depicts the distribution of trapped aromatics where the fraction of polycyclic aromatics was less (~46%, ~24% and ~57% of total anthracenes and pyrenes formed in interpellet_In_2O_3/SAPO-34, interpellet_$ZnZrO_x$/SAPO-34 and interpellet_Cr_2O_3/SAPO-34, respectively) during CO_2 hydrogenation, as compared MTO (~83% of total anthracenes and pyrenes formed in SAPO-34), indicating lower deactivation-inducing polycyclic aromatics formed during CO_2 hydrogenation. Furthermore, ^{13}C solid-state nuclear magnetic resonance (ssNMR) spectra of spent SAPO-34 and interpellet admixtures exhibited resonance at a chemical shift of 15–25 ppm for R-CH_3 or R-CH_2-R groups attached to aromatics and resonance at 125–135 ppm for alkylated and non-alkylated aromatics, as shown in **Figure 4F**.[47] Interestingly, the ratio of peak areas for aromatics to alkyl groups was higher over SAPO-34 ($A_{aromatic}/A_{alkyl} = 2.1$), as compared to interpellet admixtures ($A_{aromatic}/A_{alkyl} = 0.8$, 1.4, and 0.4 over interpellet_In_2O_3/SAPO-34, interpellet_$ZnZrO_x$/SAPO-34 and interpellet_Cr_2O_3/SAPO-34, respectively), indicating more aromatic components were present in spent SAPO-34 during MTO, as compared to CO_2 hydrogenation. Therefore, we infer that the secondary hydrogenation of olefins to paraffins in the presence of H_2, likely reduced olefin aromatization and deactivation of SAPO-34 in interpellet admixtures during CO_2 hydrogenation.

Taken together, when ion exchange of BAS did not occur in interpellet admixtures, the presence of H_2 during CO_2 hydrogenation i) favored the propagation of olefin cycle and ii) caused secondary hydrogenation of olefins to paraffins, thereby reducing olefin aromatization and the deactivation of SAPO-34.

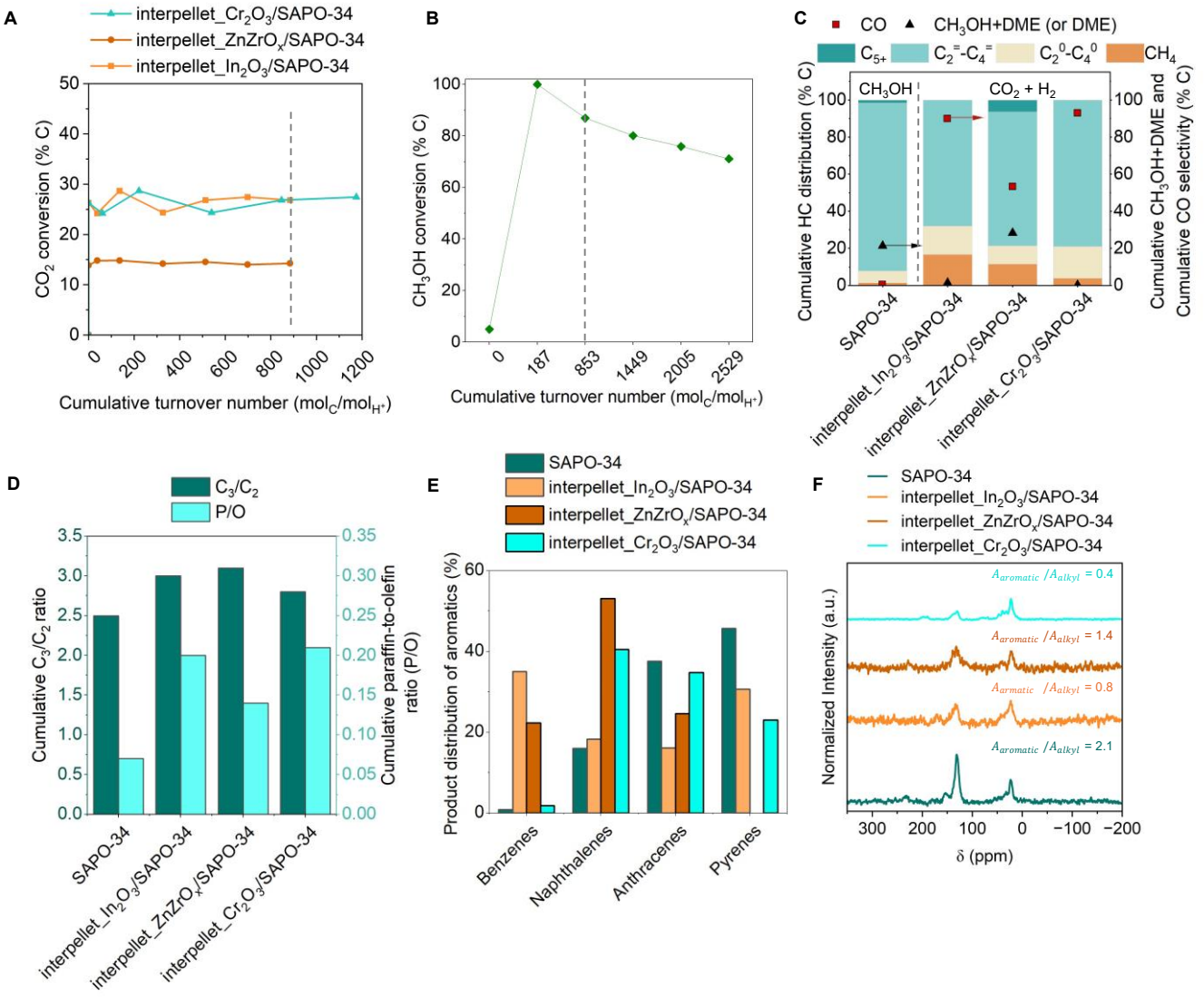

Figure 4: Catalytic performance of interpellet oxide/SAPO-34 admixtures during CO_2 hydrogenation. A) CO_2 conversion with respect to cumulative turnover number (TON) over interpellet admixture of In_2O_3, $ZnZrO_x$, Cr_2O_3 with SAPO-34. Reaction conditions: 350 °C, 500 psig, 9000 ml g_{cat}^{-1} h^{-1}, H_2:CO_2 ratio 3:1, oxide:SAPO-34 mass ratio 1:1. B) CH_3OH conversion with respect to TON over SAPO-34 during methanol-to-olefin (MTO) conversion. Reaction conditions: 350 °C, CH_3OH injection rate 0.006 ml min^{-1}, N_2 flow 75 ml min^{-1}, 0.5 g SAPO-34, total pressure 200 psig with partial pressure of CH_3OH ~6 psig. C) Cumulative hydrocarbon (HC) distribution (left axis), dimethyl ether (DME) (right axis), and CO

selectivity (right axis) during MTO over SAPO-34 and CO_2 hydrogenation over interpellet admixtures at TON ~850 mol_C/mol_{H+}. D) Cumulative C_3 (propane+propylene)/C_2 (ethane+ethylene) and paraffin-to-olefin (P/O) ratio during MTO over SAPO-34 and CO_2 hydrogenation over interpellet_In_2O_3/SAPO-34, interpellet_$ZnZrO_x$/SAPO-34, and interpellet_Cr_2O_3/SAPO-34 at TON ~850 mol_C/mol_{H+}. E) Aromatic distribution of coke species formed in SAPO-34 and interpellet admixtures. F) Solid-state ^{13}C nuclear magnetic resonance (NMR) spectra conducted over spent SAPO-34 and interpellet admixtures.

The question next arises on how the ion exchange of BAS with cations affects the reactivity of bifunctional admixtures during CO_2 hydrogenation. To explore that question, we evaluated the catalytic performance of interpellet, intrapellet, and ion-exchanged interpellet admixtures at 450 °C, 500 psig, and GHSV of 9000 ml g_{cat}^{-1} h^{-1} (**Figure 5)**. It is to be noted that at a reaction temperature of 450 °C, CH_3OH synthesis from CO_2 and H_2 is equilibrium limited (see **Figure S16**), yet we selected this reaction temperature as MTO conversion is more favored at higher reaction temperatures,[48, 49] and the combined STY of CH_3OH and HC (presuming all HC form through CH_3OH intermediate) was found to be the higher over these bifunctional systems at 450 °C, as compared to 350-400°C (see **Figure S15**).

Figure 5A shows that at a similar CO_2 conversion of ~48%, the HC distribution over intrapellet_In_2O_3/SAPO-34 (~96% CH_4 and ~4% C_2^0-C_4^0) and interpellet_In_2O_3/1.0In-SAPO-34 (~98% CH_4, ~2% C_2^0-C_4^0) shifted drastically towards CH_4 formation, as compared to interpellet_In_2O_3/SAPO-34 (~6.8% CH_4, ~29% C_2^0-C_4^0, ~61.7% olefins ($C_2^=$-$C_4^=$) and ~2.5% C_{5+}). Furthermore, the time-averaged combined space-time yield (STY) of HC and CH_3OH+DME was found to be ~10× lower over intrapellet_In_2O_3/SAPO-34 (0.4×10^{-5} mol_C g_{cat}^{-1} min^{-1}) and interpellet_In_2O_3/1.0In-SAPO-34 (0.3×10^{-5} mol_C g_{cat}^{-1} min^{-1}), as compared to interpellet_In_2O_3/SAPO-34 (3.9×10^{-5} mol_C g_{cat}^{-1} min^{-1}) (see **Figure 5B**). Hence, we infer that ion exchange of BAS with $In^{\delta+}$ reduced the number of BAS in SAPO-34 required for C-C coupling and the formation of C_{2+} HC. We reported a similar observation previously for In_2O_3/HZSM-5 system, where ion exchange of BAS with $In^{\delta+}$ inhibited the acidity of HZSM-5 and enhanced CH_4 selectivity by promoting CH_3OH hydrodeoxygenation (HDO) ($CH_3OH + H_2 \rightarrow CH_4 + H_2O$) over ion-exchanged $In^{\delta+}$ sites in the presence of H_2 during MTH.[9] Therefore, to assess if the HC distribution shifted towards CH_4 via CH_3OH HDO over $In^{\delta+}$ sites in SAPO-34, we conducted MTO over In_2O_3, 1.0In-SAPO-34, and SAPO-34, as shown in **Figure S5**. While In_2O_3 alone did not show any reactivity during MTO, 1.0In-SAPO-34 exhibited 100% CH_4 selectivity, indicating that CH_4 is likely formed over ion-exchanged $In^{\delta+}$ species *via* CH_3OH HDO.[50, 51] Previously, our DFT analysis indicated

that CH_3OH HDO likely occurs as CH_3OH adsorbs on the In_2O moiety and forms H-In-OH-In moieties in the presence of H_2 and causes hydrogenation of the methyl species to form CH_4.[9] Taken together, ion exchange of BAS with $In^{\delta+}$, inhibited the acidity of SAPO-34, and promoted CH_4 formation *via* CH_3OH HDO.

Unlike In_2O_3/SAPO-34 system, increasing the proximity of redox sites and BAS in $ZnZrO_x$/SAPO-34 system from microscale to nanoscale, improved the combined STY of HC and CH_3OH+DME (11×10^{-5} mol_C g_{cat}^{-1} min^{-1} and 19×10^{-5} mol_C g_{cat}^{-1} min^{-1} over interpellet_$ZnZrO_x$/SAPO-34 and intrapellet_$ZnZrO_x$/SAPO-34, respectively, see **Figure 5D**), at similar CO_2 conversion (~49% and ~45%, respectively, see **Figure 5C**), likely via efficient transfer and consumption of CH_3OH intermediate.[9] However, intrapellet_$ZnZrO_x$/SAPO-34 exhibited higher selectivity of CH_4 (8.7%) and C_2^0-C_4^0 (61%), as compared to interpellet_$ZnZrO_x$/SAPO-34 (1.5% CH_4 and ~28.3% C_2^0-C_4^0). This shift in HC distribution was further observed for interpellet_$ZnZrO_x$/1.0Zn-SAPO-34 (~31% CH_4 and 57% C_2^0-C_4^0), indicating ion exchange of BAS with $Zn^{\delta+}$ likely enhanced CH_4 and C_2^0-C_4^0 selectivities. This further leads to the question of how the ion exchange of BAS with $Zn^{\delta+}$ could enhance CH_4 and C_2^0-C_4^0 selectivity as the ion exchange would consequently reduce the number of BAS, which is evident from ~3× reduced STY of HC and CH_3OH+DME over interpellet_$ZnZrO_x$/1.0Zn-SAPO-34 (as compared to interpellet_$ZnZrO_x$/SAPO-34) in **Figure 5D**. Interestingly, while the combined STY reduced due to ion exchange, STY of CH_4 (1×10^{-5} mol_C g_{cat}^{-1} min^{-1}) increased and STY of C_2^0-C_4^0 (1.8×10^{-5} mol_C g_{cat}^{-1} min^{-1}) decreased over interpellet_$ZnZrO_x$/1.0Zn-SAPO-34, as compared to interpellet_$ZnZrO_x$/SAPO-34 (CH_4 ~0.1×10^{-5} mol_C g_{cat}^{-1} min^{-1} and C_2^0-C_4^0 ~3.1×10^{-5} mol_C g_{cat}^{-1} min^{-1}). These observations indicated that although $Zn^{\delta+}$ sites promoted CH_4 formation, BAS were still required for C-C coupling and C_{2+} HC formation. To further verify if $Zn^{\delta+}$ promoted CH_4 formation via CH_3OH HDO, akin to $In^{\delta+}$, we performed MTO over $ZnZrO_x$ and 1.0Zn-SAPO-34 (see **Figure S6**). Interestingly, both $ZnZrO_x$ and 1.0Zn-SAPO-34 formed CH_4 during MTO, indicating CH_3OH HDO likely occurred over the redox and $Zn^{\delta+}$ ion-exchanged sites, increasing CH_4 selectivity and STY over interpellet_$ZnZrO_x$/1.0Zn-SAPO-34.

The question then remains as to how ion exchange of BAS with $Zn^{\delta+}$ would enhance C_2^0-C_4^0 selectivity. We note that paraffin selectivity could be increased by the HT mechanism where aromatics formed inside SAPO-34 could act as hydrogen donors and/or secondary hydrogenation of olefins in the presence of unreacted H_2. Several studies reported ion exchange of BAS with $Zn^{\delta+}$ likely form $Zn^{2+}(O^-)_2$ sites, which

could act as dehydrogenation sites for olefin aromatization and subsequently enhance HT.[52-55] Additionally, H_2 spillover from $Zn^{2+}(O^{-})_2$ sites to zeolite surface (at 25-370 °C in the presence of H_2) was reported by Triwahyono *et al.* likely *via* dissociative-adsorption of molecular H_2.[40, 41] Therefore, ion exchange of BAS with $Zn^{\delta+}$ likely enhanced C_2^0-C_4^0 selectivity by HT mechanism and secondary hydrogenation of olefins in the presence of H_2 (*vide infra*).

Interestingly, for Cr_2O_3 and SAPO-34 admixtures, at a similar CO_2 conversion of ~43%, intrapellet_Cr_2O_3/SAPO-34 exhibited higher $C_2^{=}$-$C_4^{=}$ olefin selectivity (~64% $C_2^{=}$-$C_4^{=}$ in HC distribution), as compared to interpellet_Cr_2O_3/SAPO-34 (~51% $C_2^{=}$-$C_4^{=}$ in HC distribution), as shown in **Figure 5E**. However, interpellet_Cr_2O_3/1.0Cr-SAPO-34 shifted the HC distribution towards CH_4 formation (~71.7% CH_4 in HC distribution), likely via CH_3OH HDO (see **Figure S7**). Therefore, SSIE likely did not occur in intrapellet_Cr_2O_3/SAPO-34, as the HC distribution did not shift towards CH_4 formation, consistent with our XPS (**Figure 3F**) and NH_3-TPD results (**Figure 3C**). Nonetheless, intrapellet_Cr_2O_3/SAPO-34 exhibited ~2× higher STY of $C_2^{=}$-$C_4^{=}$ (1.4×10^{-5} mol_C g_{cat}^{-1} min^{-1}), as compared to interpellet_Cr_2O_3/SAPO-34 (0.74×10^{-5} mol_C g_{cat}^{-1} min^{-1}) (see **Figure 5F**), likely due to efficient transfer and consumption of CH_3OH intermediate as the distance between redox sites and BAS was reduced from ~303 μm to ~1409 nm (see **Table S2**), thereby increasing the rate of CH_3OH advection (see **Table S3**).[9] It is further to be noted that, if ion exchange occurred over intrapellet_Cr_2O_3/SAPO-34, STY of C_{2+} HC would decrease as the charge balancing protons required for C-C coupling would reduce due to ion exchange, as evident from the ~8× lower STY of C_{2+} HC over interpellet_Cr_2O_3/1.0Cr-SAPO-34 (0.24×10^{-5} mol_C g_{cat}^{-1} min^{-1}), as compared to interpellet_Cr_2O_3/SAPO-34 (2.0×10^{-5} mol_C g_{cat}^{-1} min^{-1}).

Combining these observations, we deduce that ion exchange of BAS of SAPO-34 with $In^{\delta+}$ reduced the acidity of SAPO-34 in intrapellet admixture and enhanced CH_4 selectivity via CH_3OH HDO. Similarly, partial ion exchange of BAS with $Zn^{\delta+}$ reduced the acidity of SAPO-34 in intrapellet admixture, however, $Zn^{\delta+}$ sites enhanced CH_4 selectivity via CH_3OH HDO. Additionally, $Zn^{\delta+}$ sites enhanced C_2^0-C_4^0 selectivity likely via olefin hydrogenation and/or HT mechanism (*vide infra*). Akin to $In^{\delta+}$, ion exchange of BAS with $Cr^{\delta+}$ by IWI (interpellet_Cr_2O_3/1.0Cr-SAPO-34) inhibited the acidity of SAPO-34 and reduced STY of C_{2+} HC. However, such effect was not observed in intrapellet_Cr_2O_3/SAPO-34 as likely no SSIE occurred, consistent with our NH_3-TPD and XPS analysis.

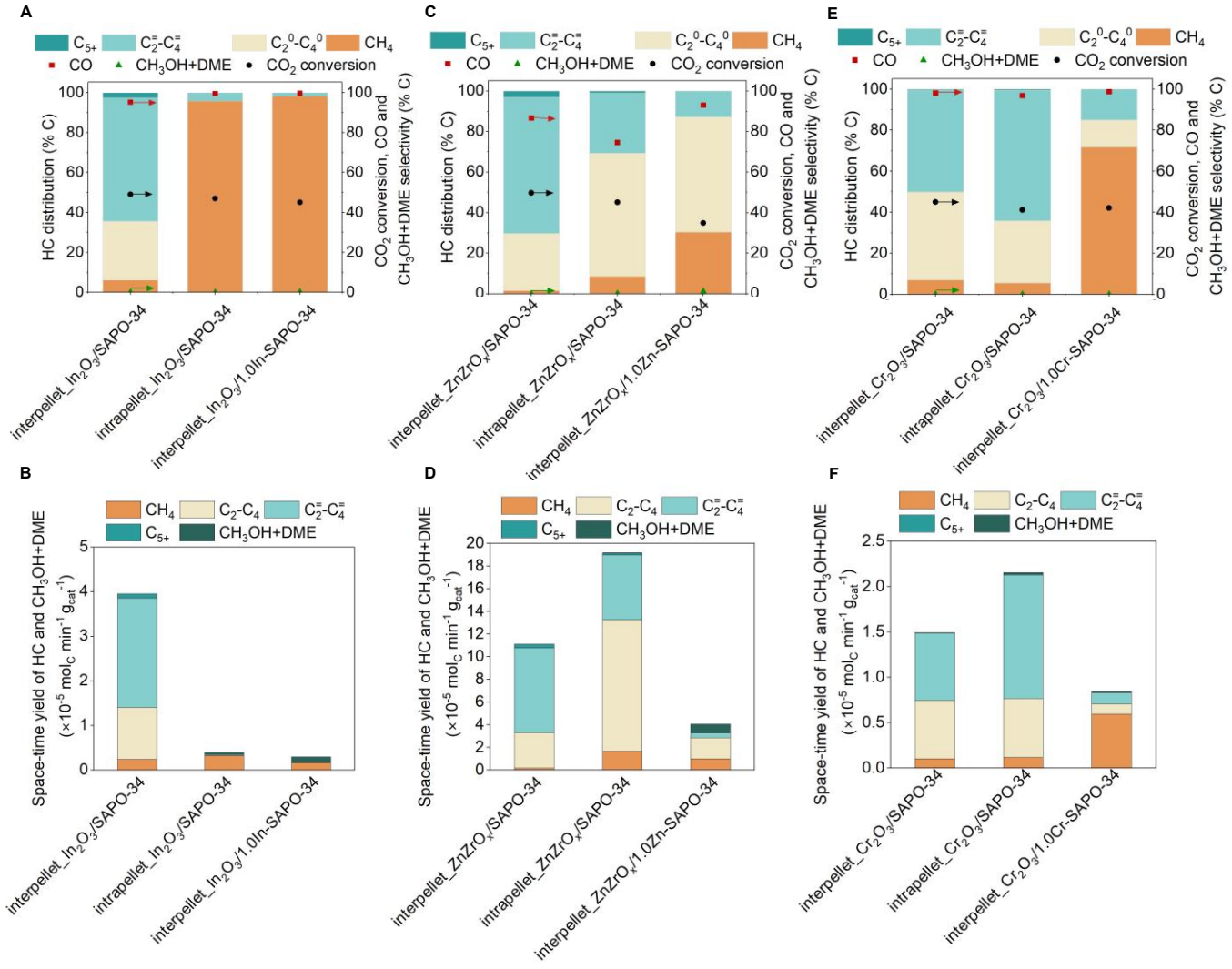

Figure 5: Probing the influence of ion exchange of Brønsted acid sites (BAS) of SAPO-34 with cations from metal oxides on the reactivity of bifunctional admixtures during CO_2 hydrogenation. A) Catalytic performance of interpellet_In_2O_3/SAPO-34, intrapellet_In_2O_3/SAPO-34, and interpellet_In_2O_3/1.0In-SAPO-34. B) Space-time-yield (STY) of HC and CH_3OH+DME over interpellet_In_2O_3/SAPO-34, intrapellet_In_2O_3/SAPO-34, and interpellet_In_2O_3/1.0In-SAPO-34 during CO_2 hydrogenation. C) Catalytic performance of interpellet_$ZnZrO_x$/SAPO-34, intrapellet_$ZnZrO_x$/SAPO-34, and interpellet_$ZnZrO_x$/1.0Zn-SAPO-34. D) STY of HC and CH_3OH+DME over interpellet_$ZnZrO_x$/SAPO-34, intrapellet_$ZnZrO_x$/SAPO-34, and interpellet_$ZnZrO_x$/1.0Zn-SAPO-34. E) Catalytic performance of interpellet_Cr_2O_3/SAPO-34, intrapellet_Cr_2O_3/SAPO-34, and interpellet_Cr_2O_3/1.0Cr-SAPO-34. F) STY of HC and CH_3OH+DME over interpellet_Cr_2O_3/SAPO-34, intrapellet_Cr_2O_3/SAPO-34, and interpellet_Cr_2O_3/1.0Cr-SAPO-34. Reaction conditions: 450 °C, 500 psig, 9000 ml g_{cat}^{-1} h^{-1}, H_2:CO_2 ratio 3:1, metal oxide:SAPO-34 mass ratio 1:1.

2.3. Probing the influence of ion-exchanged species on hydrocarbon pools (HCP)

To probe how the olefin and aromatic cycle propagation in HCP are influenced by ion exchange of BAS with cations, we evaluated the instantaneous P/O and instantaneous C_3/C_2 ratio during CO_2 hydrogenation over interpellet and intrapellet admixtures. It is to be noted that we evaluated instantaneous P/O and instantaneous C_3/C_2 ratio as minimal deactivation occurred during CO_2 hydrogenation over bifunctional oxide/SAPO-34 systems in the presence of H_2 (see **Figure S8-S10**).[9, 43] **Figure 6A** shows that both instantaneous P/O and C_3/C_2 drastically reduced over intrapellet_In_2O_3/SAPO-34 (P/O~0 as no paraffin forms, and C_3/C_2~0.6), as compared to interpellet_In_2O_3/SAPO-34 (instantaneous P/O~0.5 and instantaneous C_3/C_2~1.7). This indicates that the ion exchange of BAS with $In^{\delta+}$ likely diminished the acidity of SAPO-34 in intrapellet_In_2O_3/SAPO-34 and inhibited the propagation of the olefin and aromatic cycles. This is further evident as no C_{2+} paraffins and olefins formed over interpellet_In_2O_3/1.0In-SAPO-34, yielding P/O~0 and C_3/C_2~0. To further probe the nature of hydrocarbons formed inside the micropores of SAPO-34 during CO_2 hydrogenation, we conducted ^{13}C ssNMR (see **Figure 6B**). While resonance was observed for aromatic cycles (at ~131 ppm) and R-CH_3 or R-CH_2-R groups (at ~22 ppm) for spent interpellet_In_2O_3/SAPO-34, no resonance was observed for intrapellet_In_2O_3/SAPO-34 and interpellet_In_2O_3/1.0In-SAPO-34. This indicates that the coke formation in these cases (0.04 and 0.03 $g_{coke}/g_{catalyst}$ in spent intrapellet_In_2O_3/SAPO-34 and interpellet_In_2O_3/1.0In-SAPO-34, respectively, as compared to 0.07 $g_{coke}/g_{catalyst}$ in interpellet_In_2O_3/SAPO-34, see **Figure S35**) was minimal and likely below the detection limit of ssNMR. The ion exchange of BAS with $In^{\delta+}$ diminished the acidity of SAPO-34 which resulted in the combined STY of CH_3OH and HC to be ~10× less for intrapellet_In_2O_3/SAPO-34 and interpellet_In_2O_3/1.0In-SAPO-34, as compared to interpellet_In_2O_3/SAPO-34 (see **Figure 5B**) and consequently inhibited coking. This is again evident from the occluded HC analysis of interpellet_In_2O_3/SAPO-34, intrapellet_In_2O_3/SAPO-34 and interpellet_In_2O_3/1.0In-SAPO-34 (mass chromatogram shown in **Figure S32**). While interpellet_In_2O_3/SAPO-34 formed ~65% polycyclic aromatics (naphthalenes, anthracenes and pyrenes), intrapellet_In_2O_3/SAPO-34 and interpellet_In_2O_3/1.0In-SAPO-34 formed only ~10% and ~4% polycyclic aromatics, respectively (see **Figure 6C**), which is indicative of their inhibited acidity. Therefore, we deduce that ion exchange of BAS with $In^{\delta+}$ inhibits the propagation of HCP.

Interestingly, for $ZnZrO_x$ and SAPO-34 systems, instantaneous C_3/C_2 ratio slightly decreased over intrapellet_$ZnZrO_x$/SAPO-34 (1.9) and interpellet_$ZnZrO_x$/1.0Zn-SAPO-34 (1.8), as compared to

interpellet_$ZnZrO_x$/SAPO-34 (2.2), as shown in **Figure 6D**, indicating that the relative propagation of aromatic cycle was marginally higher when BAS were exchanged with $Zn^{\delta+}$. Furthermore, instantaneous P/O ratio increased drastically over intrapellet_$ZnZrO_x$/SAPO-34 (P/O~2) and interpellet_$ZnZrO_x$/1.0Zn-SAPO-34 (P/O~4.2), as compared to interpellet_$ZnZrO_x$/SAPO-34 (P/O~0.4), indicating that more paraffins formed due to the ion exchange of BAS with $Zn^{\delta+}$. Analysis of ^{13}C ssNMR further revealed the presence of ~3.5× more aromatic compounds with respect to alkyl groups in spent intrapellet_$ZnZrO_x$/SAPO-34 ($A_{aromatic}/A_{alkyl} = 2.5$) and interpellet_$ZnZrO_x$/1.0Zn-SAPO-34 ($A_{aromatic}/A_{alkyl} = 2.6$), as compared to interpellet_$ZnZrO_x$/SAPO-34 ($A_{aromatic}/A_{alkyl} = 0.7$), as indicated in **Figure 6E**. This is further consistent with occluded HC analysis (mass chromatogram shown in **Figure S33**) where intrapellet_$ZnZrO_x$/SAPO-34 and interpellet_$ZnZrO_x$/1.0Zn-SAPO-34 formed ~91% and ~75% polycyclic aromatics (naphthalenes, anthracenes and pyrenes), respectively, as compared to ~38% in interpellet_$ZnZrO_x$/SAPO-34 (**Figure 6F**). Combining these observations from ^{13}C ssNMR and occluded HC analysis, we infer that paraffins were likely formed by HT-mechanism where aromatics act as hydrogen-donors, hence higher selectivity of paraffins were observed over $Zn^{\delta+}$ ion-exchanged sites (in intrapellet_$ZnZrO_x$/SAPO-34 and interpellet_$ZnZrO_x$/1.0Zn-SAPO-34). However, it is to be noted that the change in P/O ratio with ion-exchanged $Zn^{\delta+}$ sites was more drastic (~5-10× higher than interpellet_$ZnZrO_x$/SAPO-34) while the change in C_3/C_2 ratio was minimal (~1.2× lower than interpellet_$ZnZrO_x$/SAPO-34). Therefore, secondary hydrogenation of olefins also likely occurred in the presence of H_2 increasing the P/O ratio.[10, 21, 38, 56] Hence, we infer that paraffins likely form both by HT mechanism and secondary hydrogenation of olefins over $Zn^{\delta+}$ sites in the presence of H_2.

Unlike the other metal oxide with SAPO-34, for Cr_2O_3 and SAPO-34 systems, instantaneous P/O and instantaneous C_3/C_2 remained similar over interpellet_Cr_2O_3/SAPO-34 (P/O~0.75 and C_3/C_2~0.77), intrapellet_Cr_2O_3/SAPO-34 (P/O~0.70 and C_3/C_2~0.73), and interpellet_Cr_2O_3/1.0Cr-SAPO-34 (P/O~0.90 and C_3/C_2~0.61), indicating olefin and aromatic cycles propagated similarly across the three systems (see **Figure 6G**). Therefore, although the $Cr^{\delta+}$ ion-exchanged sites in 1.0Cr-SAPO-34 reduced the number of BAS, they had minimal influence the relative propagation of olefin and aromatic cycles in HCP. Accordingly, ^{13}C ssNMR revealed similar ratio of aromatics to alkyl groups formed in spent interpellet_Cr_2O_3/SAPO-34 and intrapellet_Cr_2O_3/SAPO-34 ($A_{aromatic}/A_{alkyl}$ =0.5, 0.3, respectively). Consequently, occluded HC analysis (mass chromatogram shown in **Figure S34**) revealed similar fraction of polycyclic aromatics formed in spent interpellet_Cr_2O_3/SAPO-34 (~87%) and

intrapellet_Cr_2O_3/SAPO-34 (82%), as shown in **Figure 6I**. Combining these findings with the C_3/C_2 and P/O ratio, we infer that the propagation of HCP were similar over interpellet_Cr_2O_3/SAPO-34 and intrapellet_Cr_2O_3/SAPO-34, as there was likely no ion exchange of BAS with $Cr^{\delta+}$. However, for interpellet_Cr_2O_3/1.0Cr-SAPO-34, no resonance for aromatics and alkyl groups was observed by ^{13}C ssNMR (**Figure 6H**), likely due to minimal coke formation (0.04 $g_{coke}/g_{catalyst}$, shown in **Figure S35I**). This observation is further consistent with the ~8× reduced STY of C_{2+} HC over interpellet_Cr_2O_3/1.0Cr-SAPO-34 (0.24×10^{-5} mol_C g_{cat}^{-1} min^{-1}), as compared to interpellet_Cr_2O_3/SAPO-34 (2.0×10^{-5} mol_C g_{cat}^{-1} min^{-1}, see **Figure 5F**) due to having lower acid site density (as depicted in **Figure 3C**), which is also responsible for less coke formation (see **Figure S35I**).

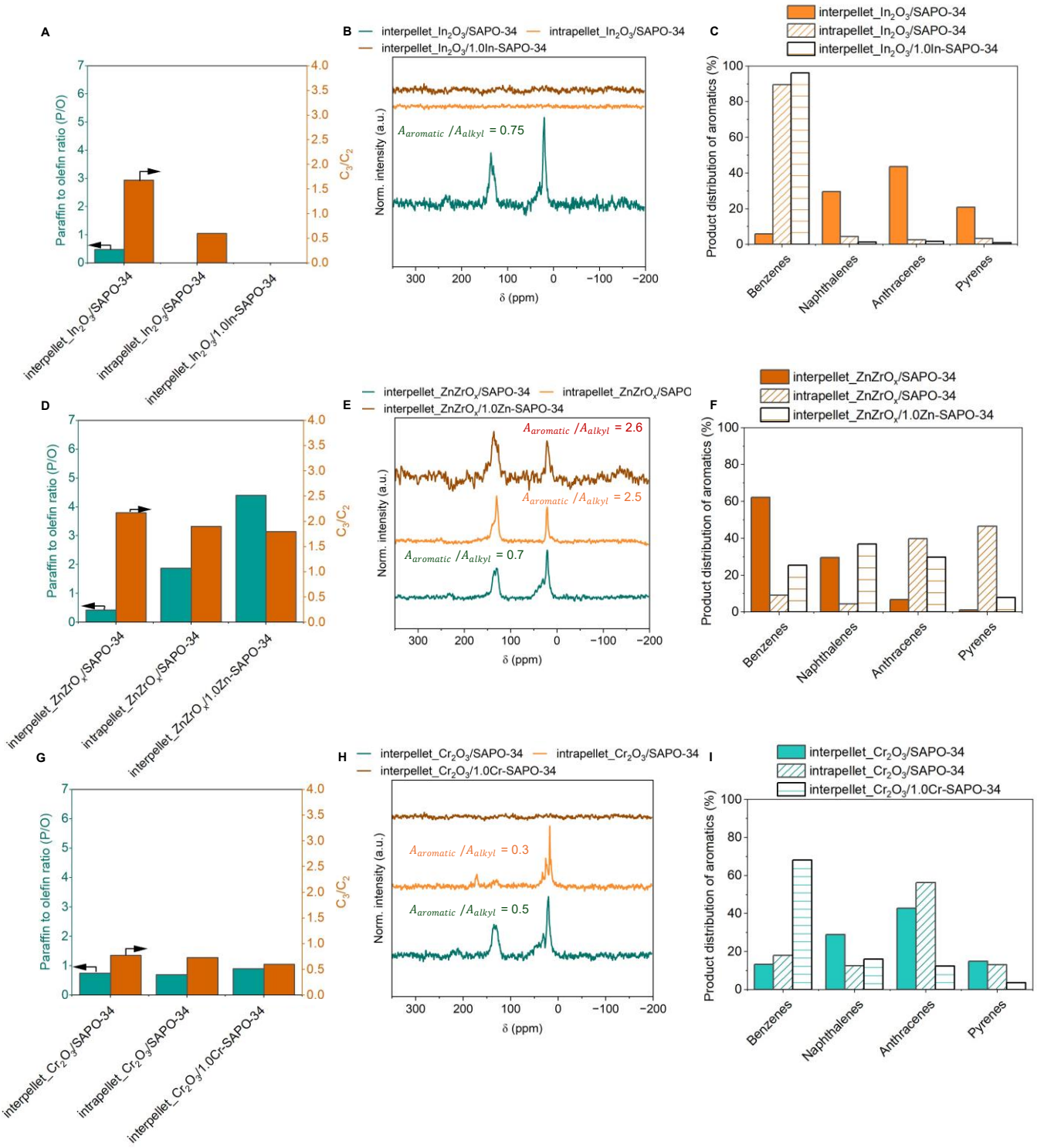

Figure 6: Probing the influence of ion-exchanged cations on hydrocarbon pools (HCP) during CO_2 hydrogenation. A) Instantaneous C_3 (propane+propylene)/C_2 (ethane+ethylene) and paraffin-to-olefin (P/O) ratio over interpellet_In_2O_3/SAPO-34, intrapellet_In_2O_3/SAPO-34 and interpellet_In_2O_3/1.0In-SAPO-34. Reaction conditions: 450 °C, 500 psig, 9000 ml g_{cat}^{-1} h^{-1}, H_2:CO_2 ratio 3:1, metal oxide:SAPO-34 mass ratio 1:1. B) ^{13}C solid-state nuclear magnetic resonance (ssNMR) spectra conducted over spent

interpellet_In_2O_3/SAPO-34, intrapellet_In_2O_3/SAPO-34 and interpellet_In_2O_3/1.0In-SAPO-34. C) Aromatic distribution of coke species formed in spent interpellet_In_2O_3/SAPO-34, intrapellet_In_2O_3/SAPO-34 and interpellet_In_2O_3/1.0In-SAPO-34. D) Instantaneous C_3/C_2 and P/O ratio over interpellet_$ZnZrO_x$/SAPO-34, intrapellet_$ZnZrO_x$/SAPO-34 and interpellet_$ZnZrO_x$/1.0Zn-SAPO-34. Reaction conditions: 450 °C, 500 psig, 9000 ml g_{cat}^{-1} h^{-1}, H_2:CO_2 ratio 3:1, metal oxide:SAPO-34 mass ratio 1:1. E) ^{13}C ssNMR spectra conducted over spent interpellet_$ZnZrO_x$/SAPO-34, intrapellet_$ZnZrO_x$/SAPO-34 and interpellet_$ZnZrO_x$/1.0Zn-SAPO-34. F) Aromatic distribution of coke species formed in spent interpellet_$ZnZrO_x$/SAPO-34, intrapellet_$ZnZrO_x$/SAPO-34 and interpellet_$ZnZrO_x$/1.0Zn-SAPO-34. G) Instantaneous C_3/C_2 and P/O ratio over interpellet_Cr_2O_3/SAPO-34, intrapellet_Cr_2O_3/SAPO-34 and interpellet_Cr_2O_3/1.0Cr-SAPO-34. Reaction conditions: 450 °C, 500 psig, 9000 ml g_{cat}^{-1} h^{-1}, H_2:CO_2 ratio 3:1, metal oxide:SAPO-34 mass ratio 1:1. H) ^{13}C ssNMR spectra conducted over spent interpellet_Cr_2O_3/SAPO-34, intrapellet_Cr_2O_3/SAPO-34 and interpellet_Cr_2O_3/1.0Cr-SAPO-34. I) Aromatic distribution of coke species formed in spent interpellet_Cr_2O_3/SAPO-34, intrapellet_Cr_2O_3/SAPO-34 and interpellet_Cr_2O_3/1.0Cr-SAPO-34.

Combining our analysis of C_3/C_2 and P/O ratios with ^{13}C ssNMR and occluded HC analysis, we conclude that ion exchange of BAS with $In^{\delta+}$ inhibited the acidity of SAPO-34 and shut down the reaction pathways for C-C coupling and propagation of HCP, as demonstrated in **Figure 7A**. Whereas, partial ion exchange of BAS with $Zn^{\delta+}$ in intrapellet_$ZnZrO_x$/SAPO-34 (acid site density 1.34 mmol/g, see **Figure 3B**) enhanced paraffin selectivity likely via HT mechanism, as demonstrated in **Figure 7B**. It is to be noted that at a higher extent of ion exchange of BAS with $Zn^{\delta+}$ as in interpellet_$ZnZrO_x$/1.0SAPO-34 (see **Figure 5D**) where the acid site density is 0.32 mmol/g (**Figure 3B**), the STY of C_{2+} HC decreased by ~3×.

For intrapellet_Cr_2O_3/SAPO-34, we did not observe ion exchange of BAS with $Cr^{\delta+}$. Therefore, instantaneous P/O and C_3/C_2 were found to be similar over interpellet and intrapellet admixtures and no influence of $Cr^{\delta+}$ was observed, as demonstrated in **Figure 7C**. However, intrapellet_Cr_2O_3/SAPO-34 exhibited ~2× higher STY of $C_2^{=}$-$C_4^{=}$ (1.4×10^{-5} mol_C g_{cat}^{-1} min^{-1}), as compared to interpellet_Cr_2O_3/SAPO-34 (0.74×10^{-5} mol_C g_{cat}^{-1} min^{-1}) (see **Figure 5F**), likely due to efficient transfer and consumption of intermediate CH_3OH. We thereby infer that advective transfer of CH_3OH dominates the catalytic performance of bifunctional oxide/zeolite systems if ion exchange of BAS does not occur.

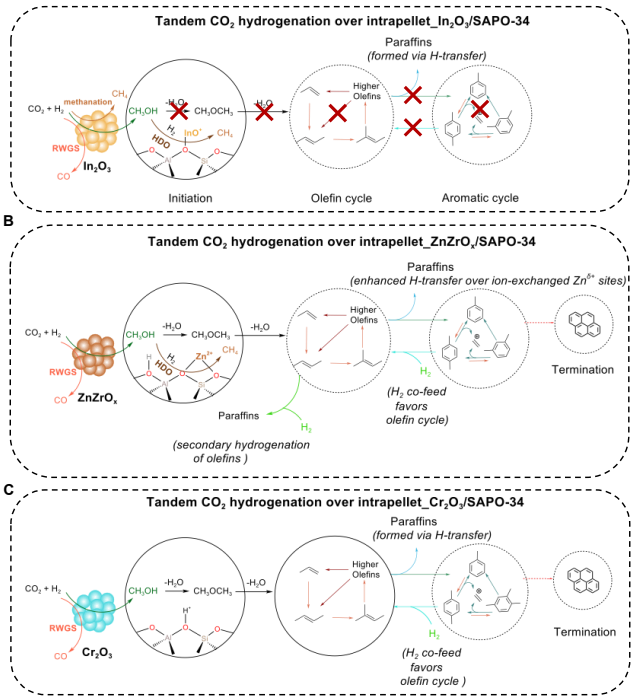

Figure 7: Illustration of the influence of ion exchange of BAS of SAPO-34 with cations (e.g., $In^{\delta+}$, $Zn^{\delta+}$, $Cr^{\delta+}$) in intrapellet admixtures on the reaction pathways during tandem CO_2 hydrogenation. A) Ion exchange of BAS with $In^{\delta+}$ diminishes the acidity of SAPO-34 and inhibits C-C coupling while promoting CH_3OH hydrodeoxygenation (HDO). B) Ion exchange of BAS with $Zn^{\delta+}$ enhanced paraffin selectivity by hydrogen transfer mechanism and secondary hydrogenation of olefins, while promoting CH_3OH HDO. C) Ion exchange between BAS and $Cr^{\delta+}$ was not observed in intrapellet_Cr_2O_3/SAPO-34, hence no influence was observed on hydrocarbon pool (HCP) propagation.

3. Conclusion

The catalytic performance of bifunctional oxide/SAPO-34 systems during CO_2 hydrogenation depend crucially on the tendency of metal oxides to form cations and their exchange with Brønsted acid sites (BAS). We estimated the likelihood of cation migration from different metal oxides (e.g., In_2O_3, $ZnZrO_x$, Cr_2O_3) by computing their metal vacancy formation energies ($Zn^{\delta+}$ (1.0 eV), $In^{\delta+}$ (3.9 eV) and $Cr^{\delta+}$ (5.8 eV)) using Density Functional Theory (DFT) calculations. These aligned with our experimental observation where we integrated these oxides with SAPO-34 at nanoscale proximity in intrapellet admixtures for solid-state ion exchange (SSIE) to occur. While SSIE of BAS with $In^{\delta+}$ and $Zn^{\delta+}$ were observed for In_2O_3/SAPO-34 and $ZnZrO_x$/SAPO-34 systems, likely no ion exchange occurred in Cr_2O_3/SAPO-34 due to its higher metal vacancy formation energy, further confirmed by NH_3-TPD. We probed the influence of these cations on the hydrocarbon pool (HCP) mechanism by evaluating propylene-to-ethylene (C_3/C_2) and paraffin-to-olefins (P/O) ratios, which indicate the relative propagation of olefin

to aromatic cycle and the degree of saturation of olefins in HCP, respectively. While $In^{\delta+}$ species diminished the acidity of SAPO-34 and inhibited HCP yielding C_3/C_2~0 and P/O~0, $Zn^{\delta+}$ species enhanced hydrogen transfer exhibiting ~5× higher P/O ratio and ~53% more polycyclic aromatics in occluded hydrocarbon distribution, as compared to its interpellet admixture where ion exchange did not transpire. Additionally, as no ion exchange occurred in Cr_2O_3/SAPO-34 system, the reactivity was influenced by the transfer of intermediate CH_3OH from redox sites to BAS. Overall, this study offers valuable insights into the nuanced influence of different cations migration and their exchange with BAS on the catalytic performance of bifunctional oxide/zeolite systems. Particularly, in the context of the HCP mechanism, these findings contribute to a deeper understanding of tandem CO_2 hydrogenation over diverse oxide/zeolite systems and underscore the importance of their rational integration.

4. Experimental Procedures

4.1. Materials

Indium (III) nitrate hydrate (99.999% metal basis, Thermo Scientific chemicals, Richardson, Texas, US) and ammonium hydroxide (28-30% NH_3 basis, Sigma-Aldrich, St. Louis, Missouri, US) were used to synthesize indium oxide (In_2O_3). Zinc nitrate hexahydrate (≥ 99%, Sigma Aldrich, St. Louis, Missouri, US) and zirconium (IV) oxynitrate hydrate (≥ 99%, Sigma Aldrich, St. Louis, Missouri, US) were used to synthesize zinc-zirconium oxide ($ZnZrO_x$). Chromium (III) nitrate nonahydrate (99.99%, Beantown Chemical, New Hampshire, US) was used to synthesize Cr_2O_3. Commercial SAPO-34 (batch 060922, SiO_2:Al_2O_3 molar ratio 0.5 with SiO_2 10wt%, Al_2O_3 42wt%, and P_2O_5 48wt%) was purchased from ACS materials. Sodium nitrate (ReagentPlus, ≥ 99%, Sigma Aldrich, St. Louis, Missouri, US) was used for ion exchange with SAPO-34.

4.2. Synthesis and preparation methods

4.2.1. Synthesis of indium oxide (In_2O_3)

Indium oxide (In_2O_3) was synthesized by the precipitation method.[10, 12] Indium (III) nitrate trihydrate ($In(NO_3)_3.3H_2O$, 5 g) was dissolved in deionized (DI) water (20 mL). The solution was added dropwise to an ammonium hydroxide (NH_4OH) solution (60 mL, 0.8 M). The as-prepared mixture was aged overnight (12 h, 70 °C) and then filtered under vacuum. The precipitate was washed with ethanol (70%), dried (5 hr), and calcined (500 °C, 4 h) with air (50 ml/min) in a muffle furnace.

4.2.2. Synthesis of zinc-zirconium oxide ($ZnZrO_x$)

Zinc-zirconium oxide ($ZnZrO_x$) was synthesized by the co-precipitation method.[10, 12] Zinc nitrate hexahydrate ($Zn(NO_3)_2.6H_2O$, 1 g) and zirconium (IV) oxynitrate ($ZrO(NO_3)_2.xH_2O$, 4 g) were dissolved in deionized (DI) water (20 mL) to have a molar ratio of Zr:Zn to be ~4:1. The solution was stirred for an hour at 70 °C. The aqueous solution was then added dropwise to an ammonium hydroxide (NH_4OH) solution (60 mL, 0.8 M). The as-prepared mixture was aged overnight (12 h, 70 °C) and then filtered under vacuum. The precipitate was washed with ethanol (70%), dried (5 hr), and calcined (500 °C, 4 h) with air (50 ml/min) in a muffle furnace.

4.2.3. Synthesis of chromium oxide (Cr_2O_3)

Chromium oxide (Cr_2O_3) was synthesized by the precipitation method.[10, 12] Chromium (III) nitrate nonahydrate ($Cr(NO_3)_3.9H_2O$, 5 g) was dissolved in deionized (DI) water (20 mL). The solution was added dropwise to an ammonium hydroxide (NH_4OH) solution (60 mL, 0.8 M). The as-prepared mixture was aged overnight (12 h, 70 °C) and then filtered under vacuum. The precipitate was washed with ethanol (70%), dried (5 hr), and calcined (500 °C, 4 h) with air (50 ml/min) in a muffle furnace.

4.2.4. SAPO-34

SAPO-34 was purchased in calcined (500 °C) form and was used directly. SAPO-34 were pretreated in the reactor bed in 5% H_2 (balance N_2) at 300°C for 1 h and cooled to 40 °C before the reaction.

4.2.5. Preparation of bifunctional metal oxide and SAPO-34 admixtures

Interpellet admixtures

Interpellet admixtures were prepared by physically mixing granules/pellets of metal oxide (e.g., In_2O_3, $ZnZrO_x$, Cr_2O_3) with granules/pellets of SAPO-34 at a mass ratio of 1:1 (total 1 g, unless otherwise specified). To prepare the granules/pellets, crystallites of metal oxide and SAPO-34 were separately pressed, crushed, and sieved into 30–60 mesh (size 250–560 μm).

Intrapellet admixtures

Intrapellet admixtures were prepared by mixing metal oxide (In_2O_3, $ZnZrO_x$, Cr_2O_3) powder with SAPO-34 crystallites in 1:1 mass ratio in an agate mortar and pestle for 15 min, followed by pressing, crushing, and sieving the mixed powder into granules of 30–60 mesh (size 250–560 μm).

4.2.6. Ion-exchange of SAPO-34

Metal ion exchanged samples (denoted as x-SAPO-34, where x=In^{3+}, Zn^{3+}, Cr^{3+}, Na^+ with x:Si molar ratio 1:1) were prepared by incipient wetness impregnation.[38] Briefly, for In-SAPO-34, a solution of $In(NO_3)_3.3H_2O$ (1.76 g in 1 ml H_2O) was added dropwise to calcined SAPO-34 (3 g, 500 °C, 4 h). The

mixture was then dried (5 hr), and calcined (500 °C, 10 h) with air (50 ml/min) in a muffle furnace. Similar procedures were used for Zn-SAPO-34, Cr-SAPO-34 and Na-SAPO-34.

4.3. Catalytic evaluation

The catalytic conversion of CO_2 hydrogenation was evaluated in a high-pressure tubular stainless steel fixed-bed reactor. The isothermal zone was ensured using a brass heating block around the reactor tube. Typically, the catalyst (1.0 g, 30-60 mesh) was first pretreated in 5% H_2 (balance N_2) at 300°C for 1 h and cooled to 40 °C prior to the reaction. The reactions were conducted at 500 psig and 350-450 °C, unless otherwise specified. Gas hourly space velocity (GHSV) was calculated using the following equation:

$$\text{GHSV} = \frac{\text{Total inlet gas flow rate (ml/h)}}{\text{total mass of the catalyst (g)}} \quad (1)$$

GHSV was maintained at 9000 ml g_{cat}^{-1} h^{-1} with a H_2:CO_2 feed ratio of 3:1 unless otherwise specified.

The products were analyzed by an online gas chromatograph (SRI-GC Multigas 5) equipped with a flame ionization detector (FID), a methanizer (FIDm), and a thermal conductivity detector (TCD). A Haysep D column was connected to the TCD and FIDm for separating and detecting CO_2, CO, CH_4, and C_2-C_4 HC, while the MXT-1 column was connected to the FID for analyzing all HC and oxygenate products (e.g., DME and CH_3OH). The outlet from the reactor was further analyzed by Agilent GCMS (8890 GC system and 5977B GC/MSD) equipped with a GasPro column connected to FID and mass spectrometer for further quantification and identification of the products. The product selectivity was calculated on a molar carbon basis. The carbon balance is given in the supplemental information (**Table S15**).

The CO_2 conversion, selectivity, and space-time-yield (STY) of products were calculated by the following equations:

$$CO_2 \text{ conversion, } X_{CO_2} = \frac{C_{CO_2,\,inlet} \cdot F_{inlet} - C_{CO_2,\,outlet} \cdot F_{outlet}}{C_{CO_2,\,inlet} \cdot F_{inlet}} \times 100\% \quad (2)$$

Where $C_{CO_2,\,inlet}$ and $C_{CO_2,\,outlet}$ are the concentrations of CO_2 at the inlet and outlet, respectively. F_{inlet} and F_{outlet} are the inlet and outlet gas flow rates of the reactor.

$$\text{Selectivity of } C_nH_m \text{ in HC distribution} = \frac{RRF_{C_nH_m} \times A_{C_nH_m}}{\sum_1^n RRF_{C_nH_m} \times A_{C_nH_m}} \times 100\% \quad (3)$$

$$\text{Selectivity of CO, } S_{CO} = \frac{RRF_{CO} \times A_{CO}}{RRF_{CO} \times A_{CO} + RRF_{CH_3OH} \times A_{CH_3OH} + RRF_{DME} \times A_{DME} + \sum_1^n RRF_{C_nH_m} \times A_{C_nH_m}} \times 100\% \quad (4)$$

$$\text{Selectivity of } CH_3OH, S_{CH_3OH} = \frac{RRF_{CH_3OH} \times A_{CH_3OH}}{RRF_{CO} \times A_{CO} + RRF_{CH_3OH} \times A_{CH_3OH} + RRF_{DME} \times A_{DME} + \sum_1^n RRF_{C_nH_m} \times A_{C_nH_m}} \times 100\% \quad (5)$$

$$\text{Selectivity of DME, } S_{DME} = \frac{RRF_{DME} \times A_{DME}}{RRF_{CO} \times A_{CO} + RRF_{CH_3OH} \times A_{CH_3OH} + RRF_{DME} \times A_{DME} + \sum_1^n RRF_{C_nH_m} \times A_{C_nH_m}} \times 100\% \quad (6)$$

$$\text{Space-time-yield (STY) of } C_nH_m = \frac{X_{CH_3OH} \times F_{CH_3OH,\,inlet} \times \left(1 - \frac{S_{CO}}{100} - \frac{S_{DME}}{100}\right) \times \text{Selectivity of } C_nH_m \text{ in HC distribution}}{[H^+]} \quad (7)$$

Where RRF is the relative response factor and A is the peak area of the species on the chromatogram. The letters n and m denote the number of C and H atoms in C_nH_m. For the catalytic performance evaluation in bar plots, the data was averaged over three points under a specific reaction condition. The carbon balance was done on a carbon mole basis. The carbon balance ranges from 97% to 101% as shown in **Table S15**.

4.4. Catalyst characterization

4.4.1. Powder X-ray diffraction (PXRD)

The PXRD patterns were acquired using a Rigaku Miniflex II X-ray instrument equipped with Cu-Kα radiation (λ=1.5406 Å). The scanning range was set from 5 to 75°, with a step rate of 0.02 and a scan rate of 1°/min.

4.4.2. Physisorption analysis

Surface area measurements were performed using the Anton Paar Autosorb iQ-C-MP EPDM automated gas sorption analyzer. The surface area analysis was carried out using Argon physisorption at 87 K, and the resulting adsorption-desorption isotherms were analyzed using the Brunauer-Emmett-Teller (BET) theory [57]. In summary, a quantity of 10-15 mg of the catalyst was placed in a 6 mm glass cell bulb (without a rod) or a 9 mm glass cell with a rod to reduce void volume. The sample underwent an initial outgassing process at 350°C for 480 min. Argon physisorption isotherm data were then collected, encompassing 72 adsorption (p/p_o values of $1e^{-6}$ to 0.995) and 27 desorption points (p/p_o values of 0.05 to 0.995). The isotherm data were subjected to BET analysis, specifically utilizing the adsorption data points ranging from p/p_o values of 0.005 to 0.3. Total pore volume was calculated based on the assumption that at relative pressures near unity, the pores filled with liquid following the equation below [58]:

$$V_{liq}=\frac{P_a V_{ads} V_m}{RT} \tag{7}$$

The micropore area and volume were calculated using the t-plot method using the deBoer thickness equation (see below) using adsorption data points ranging from p/p_o values of 0.2 to 0.5. All zeolite-containing samples contained a positive y-intercept on the t-plot indicating the presence of micropores, whereas the bulk ZnZrO and Cr_2O_3 sample's t-plot passed through the origin confirming their mesoporous identity.

$$t=\left[\frac{13.99}{\log(P_0/P)+0.034}\right]^{\frac{1}{2}} \tag{8}$$

The t-plot is a graph of the volume of gas adsorbed at STP (V_{ads}^{STP}) vs the layer thickness (t). The slope of this line (s) is related to the total surface area of the pores given by the equation below. It then follows that the micropore surface area (S_{MP}) is the difference between the BET surface area and S_t.

$$S_t\ (m^2/g) = \frac{V_{ads}^{STP}\times 15.47}{t} = s\times 15.47 \tag{9}$$

$$S_{MP} = S_{BET}-S_t \tag{10}$$

For samples without micropores, there is good agreement between S_{BET} and S_t (such is the case for bulk ZnZrO and Cr_2O_3). The micropore volume is related to the intercept (i) of this plot given by the following equation.

$$V_{MP} = i \times 0.001547\ (cm^3) \quad (11)$$

It is to be noted that for metal oxides and Cr_2O_3/SAPO-34 admixtures N_2 physisorption was employed using a similar procedure. Details on BET calculation parameters (slope and intercept) and micropore volume calculations are given in **Table S9**.

4.4.3. X-ray photoelectron spectroscopy (XPS)

X-ray photoelectron spectroscopy (XPS) measurements were conducted at the Materials Characterization Facility (MCF) located at Texas A&M University, utilizing the EnviroESCA XPS instrument.

The XPS spectra were analyzed using CasaXPS software (version 2.3.16 PR 1.5). Shirley background was selected and the C 1s spectra for adventitious carbon were used for charge correction by assigning the C-C, C-H component binding energy to 284.8 eV (See **Table S10** for additional assignments and constraints). Peak deconvolution was done using the Gaussian-Lorentzian (GL30) line shape.

The In^{3+} was assigned to 443.9 eV based on the bulk In_2O_3 spectra with a peak splitting placement of 7.54 eV and spin-orbit splitting ratio of 3:2 ($3d_{5/2}$:$3d_{3/2}$) for the 3d spectrum. 1.0In-SAPO-34 spectra were then fitted with additional components, utilizing the same splitting constraints, to account for peak broadening seen with zeolite samples compared to bulk In_2O_3 (see **Table S11**). For identification of the oxidation state of Zn species, ZnO (Zn^{2+}) peak was assigned to 1022.7 eV based on the Zn 2p spectra for the bulk ZnZrO sample. A peak splitting placement of 23 eV and a spin-orbit splitting ratio of 1:2 ($2p_{3/2}$:$2p_{1/2}$) were used for fitting $2p_{1/2}$ peaks. Additional peaks with the same constraints were used to fit zeolite samples that exhibited peak broadening. See **Table S12** for detailed fitting constraints and peak assignments. For identification of the oxidation state of Cr species in all samples, the Cr 2p spectra were collected. The Cr_2O_3 bulk spectra was used as a reference for the analysis of all subsequent zeolite samples. While the Cr 2p spectra exhibit a peaking splitting of 9.3 eV, only the $2p_{3/2}$ peak was fit as a satellite feature overlaps with the $2p_{1/2}$ peak such that fitting could lead to inaccurate analysis of species identity.[59] Cr_2O_3 $2p_{3/2}$

species shows a discrete five peak multiplet splitting as shown in **Figure 3F**. This fit is desirable compared to a single broad asymmetric peak as it allows for clearer differentiation between Cr_2O_3, $Cr(OH)_3$, and other Cr^{n+} species.[60] In addition to eliminating misassignment, the multiplet splitting allows for a more accurate count for the amount of Cr_2O_3 especially when determining the relative percentage of Cr species (Cr^0, Cr^{3+}, Cr^{6+}, etc.).[60] Additional details on fitting can be found in **Table S13**.

4.4.4. Transmission electron microscopy (TEM)

Transmission electron microscopy (TEM) analysis was conducted using the FEI TECNAI G2 F20 CRYO FE-TEM instrument, available at the Microscopy and Imaging Center (MIC) situated at Texas A&M University. Before TEM, approximately 5 mg of powder sample was added to 500 mg of isopropanol (IPA, 70% v/v, Millipore Sigma, Burlington, Massachusetts, US) and sonicated for 2 min in a water bath at room temperature. A drop of the sonicated mixture was then added to a copper grid of 200 mesh (formvar coating thickness 10 nm and carbon coating thickness 1 nm, purchased from Electron Microscopy Sciences) and dried overnight in a dryer at 50 °C.

4.4.5. Occluded hydrocarbon (HC) analysis

The occluded coke species were analyzed by digesting the spent catalyst. Briefly, 20 mg of spent catalyst was digested in 4 mL of 50 vol% H_2SO_4 aqueous solution and stirred at 60 °C for three days. The organic phase was later extracted using 3 mL of pentane (C_5) or dichloromethane (DCM) containing 0.2 mg of octadecane (C_{18}) as the internal standard. Afterward, 0.5 µL of the organic specimen was injected into the GC-MS (Agilent 8890 GC system and 5977B GC/MSD) equipped with an HP-5 column connected to FID and mass spectrometer for further quantification and identification of the products) with the following temperature program: hold for 1 min at 50 °C, then raise the temperature to 250 °C at a rate of 10 °C min^{-1}. The molecules annotated on the chromatograms were identified through fragmentation peak analysis and matching with the NIST database. The product distribution of aromatics was quantified by FID using C_{18} as the internal standard and relative response factors (RRF) for the aromatics.

4.4.6. ^{13}C solid-state nuclear magnetic resonance (ss-NMR)

The ^{13}C cross-polarization (CP) in the presence of high-power 1H decoupling (HPDEC) experiments were carried out with a Bruker Avance-NEO solid-state NMR spectrometer (400 MHz for 1H nuclei) equipped with a standard two-channel 4 mm MAS probe head. The external reference was tetramethylsilane (TMS)

for ^{13}C nuclei. The CP time for the ^{13}C NMR experiments was 1.2 ms. Approximately 50 mg sample was used for ssNMR.

4.4.7. Thermo-gravimetric analysis of spent catalyst

Temperature-programmed oxidation (TPO) of spent catalyst was conducted with TA Instruments Thermogravimetric Analyzer (TGA) Q5000 IR with infrared furnace fed with Ultra-Zero air with 100 µL platinum pans rated to 750°C (drying phase: 10°C/min ramp to 120°C followed by a 15 min isothermal phase, 20 mL/min air. TPO phase: 10°C/min ramp to 750°C, followed by a 5 min isothermal phase. Sample weight: ~5-20 mg.) The TGA curves are shown in **Figure S35**.

4.5. Computational methods

As the ion exchange requires the metal atoms from the metal oxide to migrate to the BAS in the zeolite in close contact, the likelihood of ion exchange of BAS of SAPO-34 by the metal atoms of the metal oxide was deduced based on the formation of cations from its metal oxide lattice to determine the possibility of ion exchange. The formation of cations was investigated using metal vacancy formation energy calculations using Density Functional Theory (DFT) simulations. Spin-polarized DFT simulations were performed using the Vienna *Ab initio* Simulation Package (VASP), version 5.4.4.[61] The plane wave basis set with kinetic energy cut-off energy of 450 eV (1 eV = 96.5 kJ/mol) was used for the plane wave expansion. The generalized gradient approximation of Perdew-Burke-Ernzerhof (PBE)[62] was employed to capture the electronic exchange and correlation interactions. The Projector Augmented Wave (PAW) method[63] was used for the treatment of the core-valence electron interactions. The dispersion corrections were incorporated using Grimme's DFT-D3 method implemented in VASP to account for the dispersion interactions in the DFT calculations.[64] The geometries were fully relaxed until the residual forces were smaller than 0.1 eV/Å, and the self-consistent energy convergence was set to 1.0×10^{-4} eV/atom. For more details on the methods adopted, please refer to supplemental **section S2.4** in the supplemental information.

Acknowledgments

We are grateful to the Artie McFerrin Department of Chemical Engineering at Texas A&M University, the College of Engineering, Dr. Mark Barteau, and the Provost for their financial support. This work was funded by Texas A&M University (TAMU), Texas A&M Engineering Experiment Station (TEES), the Governor's University Research Initiative (GURI), the Oak Ridge Associated Universities through their

Ralph E. Powe Junior Faculty Enhancement Award, and the National Science Foundation (NSF) CBET grant number 2245474. MS acknowledges partial support from Texas A&M University System's National Laboratory Office (NLO) for their Development Fellowship. We thank Dr. Yu-Ting Lin and Prof. Mustafa Akbulut for their assistance with collecting transmission electron microscopy (TEM). We thank Mr. Ryan Helmer for their assistance with the construction and maintenance of H_2-TPR system. We also acknowledge that the XPS characterization of the catalyst powders was performed in the Texas A&M University Materials Characterization Core Facility (RRID:SCR_022202), TEM characterization was performed at Texas A&M University Microscopy and Imaging Center (MIC) (RRID:SCR_022128). BCD and JJV acknowledge the support of the Carbon Capture Utilization and Storage (CCUS) Centre of Excellence at the Indian Institute of Technology Madras.

Authors Contributions

F.M., J.M., and M.S. – conceptualization. F.M. – writing-original draft. F.M. and J.M. – data collection and analysis. B.D. and J.J.V. – DFT calculations and analysis, J.V. – XPS and physisorption data collection and analysis. F.M., J.J.V., and M.S. – writing-review and editing. M.S - Funding acquisition and supervision. All authors contributed to the manuscript.

Declaration of interests

The authors declare no competing interests.

References

(1) Bollini, P.; Diwan, M.; Gautam, P.; Hartman, R. L.; Hickman, D. A.; Johnson, M.; Kawase, M.; Neurock, M.; Patience, G. S.; Stottlemyer, A. Vision 2050: Reaction Engineering Roadmap. *ACS Engineering Au* **2023**, *3* (6), 364-390.

(2) Livescu, A.; Navar, R.; Mangalindan, J. R.; Mahnaz, F.; Ge, Y.; Shetty, M.; Yang, X. Catalysts for Clean Energy: A Review on Current Progress for the Catalyzed Recycling of CO2 into Dimethyl Ether. *Topics in Catalysis* **2024**, 1-22.

(3) Mahnaz, F.; Dunlap, V.; Helmer, R.; Borkar, S. S.; Navar, R.; Yang, X.; Shetty, M. Selective Valorization of CO2 towards Valuable Hydrocarbons through Methanol-mediated Tandem Catalysis. *ChemCatChem* **2023**, *15* (17), e202300402.

(4) Ji, Q.; Li, D.; Hu, J.; Gao, P.; Hou, G.; Liu, Y.; Deng, D. Direct synthesis of iso-olefins from carbon dioxide hydrogenation via tandem catalysis. *Cell Reports Physical Science* **2024**.

(5) Sharma, P.; Sebastian, J.; Ghosh, S.; Creaser, D.; Olsson, L. Recent advances in hydrogenation of CO 2 into hydrocarbons via methanol intermediate over heterogeneous catalysts. *Catalysis Science & Technology* **2021**, *11* (5), 1665-1697.

(6) Wang, Y.; Tan, L.; Tan, M.; Zhang, P.; Fang, Y.; Yoneyama, Y.; Yang, G.; Tsubaki, N. Rationally designing bifunctional catalysts as an efficient strategy to boost CO2 hydrogenation producing value-added aromatics. *Acs Catalysis* **2018**, *9* (2), 895-901.

(7) Gambo, Y.; Adamu, S.; Lucky, R. A.; Ba-Shammakh, M. S.; Hossain, M. M. Tandem catalysis: A sustainable alternative for direct hydrogenation of CO2 to light olefins. *Applied Catalysis A: General* **2022**, *641*, 118658.

(8) Wang, Y.; Gao, X.; Wu, M.; Tsubaki, N. Thermocatalytic hydrogenation of CO2 into aromatics by tailor-made catalysts: Recent advancements and perspectives. *EcoMat* **2021**, *3* (1), e12080.

(9) Mahnaz, F.; Mangalindan, J. R.; Dharmalingam, B. C.; Vito, J.; Lin, Y.-T.; Akbulut, M.; Varghese, J. J.; Shetty, M. Intermediate Transfer Rates and Solid-State Ion Exchange are Key Factors Determining the Bifunctionality of In2O3/HZSM-5 Tandem CO2 Hydrogenation Catalyst. *ACS Sustainable Chemistry & Engineering* **2024**.

(10) Wang, Y.; Wang, G.; van der Wal, L. I.; Cheng, K.; Zhang, Q.; de Jong, K. P.; Wang, Y. Visualizing Element Migration over Bifunctional Metal-Zeolite Catalysts and its Impact on Catalysis. *Angewandte Chemie* **2021**, *133* (32), 17876-17884.

(11) Tan, K. B.; Xu, K.; Cai, D.; Huang, J.; Zhan, G. Rational design of bifunctional catalysts with proper integration manners for CO and CO2 hydrogenation into value-added products: A review. *Chemical Engineering Journal* **2023**, *463*, 142262.

(12) Gao, P.; Li, S.; Bu, X.; Dang, S.; Liu, Z.; Wang, H.; Zhong, L.; Qiu, M.; Yang, C.; Cai, J. Direct conversion of CO2 into liquid fuels with high selectivity over a bifunctional catalyst. *Nature chemistry* **2017**, *9* (10), 1019-1024.

(13) Xie, T.; Ding, J.; Shang, X.; Zhang, X.; Zhong, Q. Effective synergies in indium oxide loaded with zirconia mixed with silicoaluminophosphate molecular sieve number 34 catalysts for carbon dioxide hydrogenation to lower olefins. *Journal of Colloid and Interface Science* **2023**, *635*, 148-158.

(14) Gao, P.; Dang, S.; Li, S.; Bu, X.; Liu, Z.; Qiu, M.; Yang, C.; Wang, H.; Zhong, L.; Han, Y. Direct production of lower olefins from CO2 conversion via bifunctional catalysis. *ACS Catal.* **2018**, *8* (1), 571-578.

(15) Li, Y.; Zeng, L.; Pang, G.; Wei, X.; Wang, M.; Cheng, K.; Kang, J.; Serra, J. M.; Zhang, Q.; Wang, Y. Direct conversion of carbon dioxide into liquid fuels and chemicals by coupling green hydrogen at high temperature. *Appl. Catal., B* **2023**, *324*, 122299.

(16) Xing, S.; Turner, S.; Fu, D.; van Vreeswijk, S.; Liu, Y.; Xiao, J.; Oord, R.; Sann, J.; Weckhuysen, B. M. Silicalite-1 layer secures the bifunctional nature of a CO2 hydrogenation catalyst. *JACS Au* **2023**, *3* (4), 1029-1038.

(17) Wang, G.; Wang, Y.; Cao, J.; Wang, X.; Yi, Y.; Liu, F. Fabrication of ZnZrO2@ Al2O3@ SAPO-34 tandem catalyst for CO2 conversion to hydrocarbons. *Microporous and Mesoporous Materials* **2020**, *291*, 109693.

(18) Wang, J.; Li, R.; Zhang, G.; Dong, C.; Fan, Y.; Yang, S.; Chen, M.; Guo, X.; Mu, R.; Ning, Y. Confinement-Induced Indium Oxide Nanolayers Formed on Oxide Support for Enhanced CO2 Hydrogenation Reaction. *Journal of the American Chemical Society* **2024**.

(19) Ilias, S.; Bhan, A. Mechanism of the catalytic conversion of methanol to hydrocarbons. *ACS Catal.* **2013**, *3* (1), 18-31.
(20) Ono, Y.; Adachi, H.; Senoda, Y. Selective conversion of methanol into aromatic hydrocarbons over zinc-exchanged ZSM-5 zeolites. *Journal of the Chemical Society, Faraday Transactions 1: Physical Chemistry in Condensed Phases* **1988**, *84* (4), 1091-1099.
(21) Esquivel, D.; Cruz-Cabeza, A. J.; Jimenez-Sanchidrian, C.; Romero-Salguero, F. J. Transition metal exchanged β zeolites: Characterization of the metal state and catalytic application in the methanol conversion to hydrocarbons. *Microporous and mesoporous materials* **2013**, *179*, 30-39.
(22) Ilias, S.; Bhan, A. Tuning the selectivity of methanol-to-hydrocarbons conversion on H-ZSM-5 by co-processing olefin or aromatic compounds. *Journal of catalysis* **2012**, *290*, 186-192.
(23) Tada, S.; Kinoshita, H.; Ochiai, N.; Chokkalingam, A.; Hu, P.; Yamauchi, N.; Kobayashi, Y.; Iyoki, K. Search for solid acid catalysts aiming at the development of bifunctional tandem catalysts for the one-pass synthesis of lower olefins via CO2 hydrogenation. *International Journal of Hydrogen Energy* **2021**, *46* (74), 36721-36730.
(24) LU, S.-y.; YANG, H.-y.; YANG, C.-g.; Peng, G.; SUN, Y.-h. Highly selective synthesis of LPG from CO2 hydrogenation over In2O3/SSZ-13 binfunctional catalyst. *Journal of Fuel Chemistry and Technology* **2021**, *49* (8), 1132-1139.
(25) Gao, J.; Jia, C.; Liu, B. Direct and selective hydrogenation of CO 2 to ethylene and propene by bifunctional catalysts. *Catalysis Science & Technology* **2017**, *7* (23), 5602-5607.
(26) Tian, P.; Zhan, G.; Tian, J.; Tan, K. B.; Guo, M.; Han, Y.; Fu, T.; Huang, J.; Li, Q. Direct CO2 hydrogenation to light olefins over ZnZrOx mixed with hierarchically hollow SAPO-34 with rice husk as green silicon source and template. *Applied Catalysis B: Environmental* **2022**, *315*, 121572.
(27) Dang, S.; Gao, P.; Liu, Z.; Chen, X.; Yang, C.; Wang, H.; Zhong, L.; Li, S.; Sun, Y. Role of zirconium in direct CO2 hydrogenation to lower olefins on oxide/zeolite bifunctional catalysts. *Journal of catalysis* **2018**, *364*, 382-393.
(28) Gao, P.; Dang, S.; Li, S.; Bu, X.; Liu, Z.; Qiu, M.; Yang, C.; Wang, H.; Zhong, L.; Han, Y. Direct production of lower olefins from CO2 conversion via bifunctional catalysis. *ACS Catalysis* **2018**, *8* (1), 571-578.
(29) Li, Z.; Wang, J.; Qu, Y.; Liu, H.; Tang, C.; Miao, S.; Feng, Z.; An, H.; Li, C. Highly selective conversion of carbon dioxide to lower olefins. *Acs Catalysis* **2017**, *7* (12), 8544-8548.
(30) Tan, L.; Zhang, P.; Cui, Y.; Suzuki, Y.; Li, H.; Guo, L.; Yang, G.; Tsubaki, N. Direct CO2 hydrogenation to light olefins by suppressing CO by-product formation. *Fuel Processing Technology* **2019**, *196*, 106174.
(31) Li, J.; Yu, T.; Miao, D.; Pan, X.; Bao, X. Carbon dioxide hydrogenation to light olefins over ZnO-Y2O3 and SAPO-34 bifunctional catalysts. *Catalysis Communications* **2019**, *129*, 105711.
(32) Ghasemi, M.; Mohammadi, M.; Sedighi, M. Sustainable production of light olefins from greenhouse gas CO2 over SAPO-34 supported modified cerium oxide. *Microporous and Mesoporous Materials* **2020**, *297*, 110029.
(33) Liu, Z.; Ni, Y.; Sun, T.; Zhu, W.; Liu, Z. Conversion of CO2 and H2 into propane over InZrOx and SSZ-13 composite catalyst. *Journal of Energy Chemistry* **2021**, *54*, 111-117.
(34) Chen, J.; Wang, X.; Wu, D.; Zhang, J.; Ma, Q.; Gao, X.; Lai, X.; Xia, H.; Fan, S.; Zhao, T.-S. Hydrogenation of CO2 to light olefins on CuZnZr@(Zn-) SAPO-34 catalysts: Strategy for product distribution. *Fuel* **2019**, *239*, 44-52.
(35) Shi, Z.; Bhan, A. Metrics of performance relevant in methanol-to-hydrocarbons catalysis. *Journal of Catalysis* **2023**, *421*, 198-209.
(36) Li, Y.; Wang, M.; Liu, S.; Wu, F.; Zhang, Q.; Zhang, S.; Cheng, K.; Wang, Y. Distance for communication between metal and acid sites for syngas conversion. *ACS Catalysis* **2022**, *12* (15), 8793-8801.
(37) Gabrienko, A. A.; Arzumanov, S. S.; Moroz, I. B.; Prosvirin, I. P.; Toktarev, A. V.; Wang, W.; Stepanov, A. G. Methane activation on in-modified ZSM-5: the state of indium in the zeolite and pathways of methane transformation to surface species. *The Journal of Physical Chemistry C* **2014**, *118* (15), 8034-8043.
(38) Niu, X.; Gao, J.; Miao, Q.; Dong, M.; Wang, G.; Fan, W.; Qin, Z.; Wang, J. Influence of preparation method on the performance of Zn-containing HZSM-5 catalysts in methanol-to-aromatics. *Microporous and Mesoporous Materials* **2014**, *197*, 252-261.

(39) Gabrienko, A. A.; Arzumanov, S. S.; Toktarev, A. V.; Danilova, I. G.; Prosvirin, I. P.; Kriventsov, V. V.; Zaikovskii, V. I.; Freude, D.; Stepanov, A. G. Different efficiency of Zn2+ and ZnO species for methane activation on Zn-modified zeolite. *ACS Catalysis* **2017**, *7* (3), 1818-1830.
(40) Triwahyono, S.; Jalil, A. A.; Mukti, R. R.; Musthofa, M.; Razali, N. A. M.; Aziz, M. A. A. Hydrogen spillover behavior of Zn/HZSM-5 showing catalytically active protonic acid sites in the isomerization of n-pentane. *Applied Catalysis A: General* **2011**, *407* (1-2), 91-99.
(41) Kamarudin, N. H. N.; Jalil, A. A.; Triwahyono, S.; Mukti, R. R.; Ab Aziz, M. A.; Setiabudi, H. D.; Muhid, M. N. M.; Hamdan, H. Interaction of Zn2+ with extraframework aluminum in HBEA zeolite and its role in enhancing n-pentane isomerization. *Applied Catalysis A: General* **2012**, *431*, 104-112.
(42) Redekop, E. A.; Cordero-Lanzac, T.; Salusso, D.; Pokle, A.; Oien-Odegaard, S.; Sunding, M. F.; Diplas, S.; Negri, C.; Borfecchia, E.; Bordiga, S. Zn Redistribution and Volatility in ZnZrO x Catalysts for CO2 Hydrogenation. *Chemistry of Materials* **2023**, *35* (24), 10434-10445.
(43) Mahnaz, F.; Mangalindan, J.; Vito, J.; Helmer, R.; Shetty, M. Influence of Acid Strength on Olefin Selectivity of Chabazite (CHA) Framework Zeolite/Zeotypes during Tandem CO2 Hydrogenation. *Journal of Catalysis* **2024**, *Volume 434, 115518*.
(44) Kozuch, S.; Martin, J. M. "Turning over" definitions in catalytic cycles. ACS Publications: 2012; Vol. 2, pp 2787-2794.
(45) Shi, Z.; Bhan, A. The effects of CO co-feed on the catalytic performance of Methanol-to-Hydrocarbons conversion on HZSM-5. *Chemical Engineering Journal* **2023**, *456*, 140867.
(46) Arora, S. S.; Shi, Z.; Bhan, A. Mechanistic basis for effects of high-pressure H2 cofeeds on methanol-to-hydrocarbons catalysis over zeolites. *ACS Catalysis* **2019**, *9* (7), 6407-6414.
(47) Jiang, Y.; Huang, J.; Marthala, V. R.; Ooi, Y. S.; Weitkamp, J.; Hunger, M. In situ MAS NMR–UV/Vis investigation of H-SAPO-34 catalysts partially coked in the methanol-to-olefin conversion under continuous-flow conditions and of their regeneration. *Microporous and Mesoporous Materials* **2007**, *105* (1-2), 132-139.
(48) Yarulina, I.; Chowdhury, A. D.; Meirer, F.; Weckhuysen, B. M.; Gascon, J. Recent trends and fundamental insights in the methanol-to-hydrocarbons process. *Nat. Catal.* **2018**, *1* (6), 398-411.
(49) Keil, F. J. Methanol-to-hydrocarbons: process technology. *Microporous and mesoporous materials* **1999**, *29* (1-2), 49-66.
(50) Zhao, W.; Zhang, B.; Wang, G.; Guo, H. Methane formation route in the conversion of methanol to hydrocarbons. *Journal of energy chemistry* **2014**, *23* (2), 201-206.
(51) Sackers, N. M.; Nikodemus, J.; Palkovits, R.; Sautet, P.; Hausoul, P. J. Ru-Catalyzed Hydrogenolysis of Methanol: A Computational and Kinetics Study. *ChemCatChem* **2023**, *15* (9), e202201530.
(52) Mehdad, A.; Lobo, R. F. Ethane and ethylene aromatization on zinc-containing zeolites. *Catalysis Science & Technology* **2017**, *7* (16), 3562-3572.
(53) Li, Y.; Liu, S.; Xie, S.; Xu, L. Promoted metal utilization capacity of alkali-treated zeolite: Preparation of Zn/ZSM-5 and its application in 1-hexene aromatization. *Applied Catalysis A: General* **2009**, *360* (1), 8-16.
(54) Chen, X.; Dong, M.; Niu, X.; Wang, K.; Chen, G.; Fan, W.; Wang, J.; Qin, Z. Influence of Zn species in HZSM-5 on ethylene aromatization. *Chinese Journal of Catalysis* **2015**, *36* (6), 880-888.
(55) Geng, R.; Liu, Y.; Guo, Y.; Wang, P.; Dong, M.; Wang, S.; Wang, J.; Qin, Z.; Fan, W. Structure evolution of Zn species on fresh, deactivated, and regenerated Zn/ZSM-5 catalysts in ethylene aromatization. *ACS Catalysis* **2022**, *12* (23), 14735-14747.
(56) Liu, J.; He, N.; Zhou, W.; Lin, L.; Liu, G.; Liu, C.; Wang, J.; Xin, Q.; Xiong, G.; Guo, H. Isobutane aromatization over a complete Lewis acid Zn/HZSM-5 zeolite catalyst: performance and mechanism. *Catalysis Science & Technology* **2018**, *8* (16), 4018-4029.
(57) Brunauer, S.; Emmett, P. H.; Teller, E. Adsorption of Gases in Multimolecular Layers. *Journal of the American Chemical Society* **1938**, *60* (2), 309-319. DOI: 10.1021/ja01269a023.
(58) Anton Paar QuantaTec, I. Instruction Manual and Safety Information. In *autosorb iQ Gas Sorption System*, Graz, Austria, 2022.
(59) Payne, B.; Biesinger, M.; McIntyre, N. X-ray photoelectron spectroscopy studies of reactions on chromium metal and chromium oxide surfaces. *Journal of Electron Spectroscopy and Related Phenomena* **2011**, *184* (1-2), 29-37.

(60) Biesinger, M. C.; Payne, B. P.; Grosvenor, A. P.; Lau, L. W.; Gerson, A. R.; Smart, R. S. C. Resolving surface chemical states in XPS analysis of first row transition metals, oxides and hydroxides: Cr, Mn, Fe, Co and Ni. *Applied Surface Science* **2011**, *257* (7), 2717-2730.
(61) Kresse, G.; Furthmüller, J. Efficient iterative schemes for ab initio total-energy calculations using a plane-wave basis set. *Physical review B* **1996**, *54* (16), 11169.
(62) Perdew, J. P.; Burke, K.; Ernzerhof, M. Generalized gradient approximation made simple. *Physical review letters* **1996**, *77* (18), 3865.
(63) Kresse, G.; Joubert, D. From ultrasoft pseudopotentials to the projector augmented-wave method. *Physical review b* **1999**, *59* (3), 1758.
(64) Grimme, S.; Antony, J.; Ehrlich, S.; Krieg, H. A consistent and accurate ab initio parametrization of density functional dispersion correction (DFT-D) for the 94 elements H-Pu. *The Journal of chemical physics* **2010**, *132* (15).

Influence of nanoscale proximity between redox sites and Brønsted acid sites on tandem CO_2 hydrogenation